Fate of trace elements in Oxygen Carrier Aided Combustion (OCAC) of municipal solid waste

Fuel xxx (xxxx) xxx

Contents lists available at ScienceDirect

Fuel

journal homepage: www.elsevier.com/locate/fuel

Full Length Article

Fate of trace elements in Oxygen Carrier Aided Combustion (OCAC) of municipal solid waste

Ivana Staničić [a,*], Rainer Backman [b], Yu Cao [c], Magnus Rydén [a], Jesper Aronsson [a], Tobias Mattisson [a]

[a] Department of Space, Earth and Environment, Division of Energy Technology, Chalmers University of Technology, SE-412 96 Gothenburg, Sweden
[b] Department of Applied Physics and Electronics, Thermochemical Energy Conversion Laboratory, Umeå University, SE 901 87 Umeå, Sweden
[c] Department of Industrial and Materials Science, Chalmers University of Technology, SE-412 96 Gothenburg, Sweden

ARTICLE INFO

Keywords:
Oxygen carrier
Oxygen Carrier Aided Combustion (OCAC)
Ilmenite
Municipal solid waste (MSW)
X-Ray Photoelectron Spectroscopy (XPS)
Thermodynamic equilibrium calculation

ABSTRACT

Oxygen Carrier Aided Combustion is a novel fluidized bed concept for burning waste. This study analyzed solid samples from an industrial OCAC application using municipal solid waste and the oxygen carrier ilmenite. The presence of oxygen carriers impacts the ash chemistry, which can influence corrosion and ash characteristics. By investigating samples obtained from industrial applications, unique and highly relevant information on the solid-state chemistry and the fate of important elements can be obtained. In total, 20 bottom ashes and 17 fly ashes were sampled over a period of 38 days. In a preceding study, the surface interaction between ilmenite and Zn, Cu and Pb was investigated. In this paper, the distribution of these elements throughout the particle cross-section and the influence of residence time has been studied using XRD, SEM-EDX and XPS. The results show that Zn is incorporated in the Fe-rich ash layer over time in the form of Zn ferrites, while Cu accumulates inside the ilmenite particles with time, and Cr is enriched in the magnetically separated bottom ash. Low concentrations of Pb were detected in the bottom ashes, suggesting that a significant part is released in the gas phase. The influence of temperature, bed material and reduction potential were evaluated using multicomponent, multiphase equilibrium calculations. It is shown that an ilmenite bed is less prone to form melts in comparison to a bed of silica sand and that the addition of sulfur could decrease the volatilization of Pb.

1. Introduction

The concentrations of greenhouse gases in the atmosphere are increasing as a result of anthropogenic activities. The main reason is the extensive use of fossil fuels [1]. Consequently, the global mean temperature has increased with subsequent climate change. The warming from these anthropogenic emissions will persist from centuries to millennia and cause long-term changes in the climate system [2]. It is necessary to remove carbon dioxide from the atmosphere to reach the climate goals and limit the increase to below 2 °C [3].

The second-largest contributor to greenhouse gas emissions is methane, which has a global warming potential of $GWP_{100} = 28$ [3,4]. One of the largest anthropogenic sources of methane emissions originates from waste landfills [5]. When municipal solid waste (MSW) is landfilled, the biodegradable portion releases methane and CO_2 into the atmosphere. Since the beginning of the 21st century, the disposal of waste in landfills in the EU has been reduced by more than half due to the Waste Framework Directive (Directive 2008/98/EC) and Landfill Directive (Council Directive 1999/31/EC). Furthermore, recycling and composting of solid waste have increased by a factor of three, and incineration with energy recovery has increased fourfold [6].

Global waste generation is expected to increase from 2.01 billion tons (2016) to 3.40 billion tons by 2050 [7,8], which may be attributed to increasing population along with economic growth [7]. In addition, the global Waste-to-Energy (WtE) technology markets can be expected to grow drastically along with the increasing energy demand. This will require the handling of large volumes of waste, the incineration of which provides renewable energy benefits while causing less GHG emissions as compared to landfilling [3]. It will also decrease the volume of waste flows by 70 wt% and is beneficial from a hygienic point of view [9]. It would be further advantageous if WtE is combined with Carbon Capture and Storage (CCS) since utilizing biomass for combustion provides a possibility for carbon–neutral or even negative emissions, which is fundamental to achieve climate goals [10,11].

* Corresponding author.
E-mail address: stanicic@chalmers.se (I. Staničić).

https://doi.org/10.1016/j.fuel.2021.122551
Received 9 June 2021; Received in revised form 25 August 2021; Accepted 7 November 2021

WtE technologies allow the conversion of waste to valuable products such as electricity, heat, fuels, chemicals, and fertilizers. Some European countries, such as Sweden, have adapted advanced waste management technologies to reduce waste disposal, while also producing electricity and heat. Sweden has 37 waste combustion facilities that annually receive around six million tons of waste, containing high fractions of bio-based material such as wood and paper [12]. One of the leading energy recovery technologies is fluidized bed combustion, which is suitable for biomass combustion as it can handle a wide range of fuels. One technology based on fluidized bed combustion, is Oxygen Carrier Aided Combustion (OCAC), see Fig. 1. OCAC is realized by replacing the commonly used inert material, such as silica sand, that makes up the fluidized bed, with an oxygen carrier (OC). The oxygen carrier is an active bed material, usually in the form of metal oxides (Me_xO_y). This replacement of bed material has several advantages. The active bed material will be reduced in fuel-rich parts of the bed and oxidized in oxygen-rich parts, leading to a more even oxygen availability and temperature in the boiler [13,14]. Additionally, it can increase both combustion efficiency and capacity [14]. It has also been shown to reduce the risk for agglomeration and has positive effects on emissions levels [15]. The OCAC-concept has been successfully operated in industrial facilities, using ilmenite as bed material. Still, research about the technology is relatively limited [14,16,17]. There are several reasons why it is essential to study OCAC scientifically and, more specifically, the interactions of oxygen carrier and ash material: i) The presence of oxygen carriers will likely have a significant impact on ash-chemistry compared to silica sand, which can affect agglomeration and corrosion as well as final ash characteristics [18,19], ii) cost of oxygen carriers may exceed that of silica sand, and thus it is important to limit ash-induced deactivation of the material, and iii) OCAC can be seen as the first step towards implementation of chemical-looping combustion (CLC); a carbon capture technology which also utilizes oxygen carriers [20].

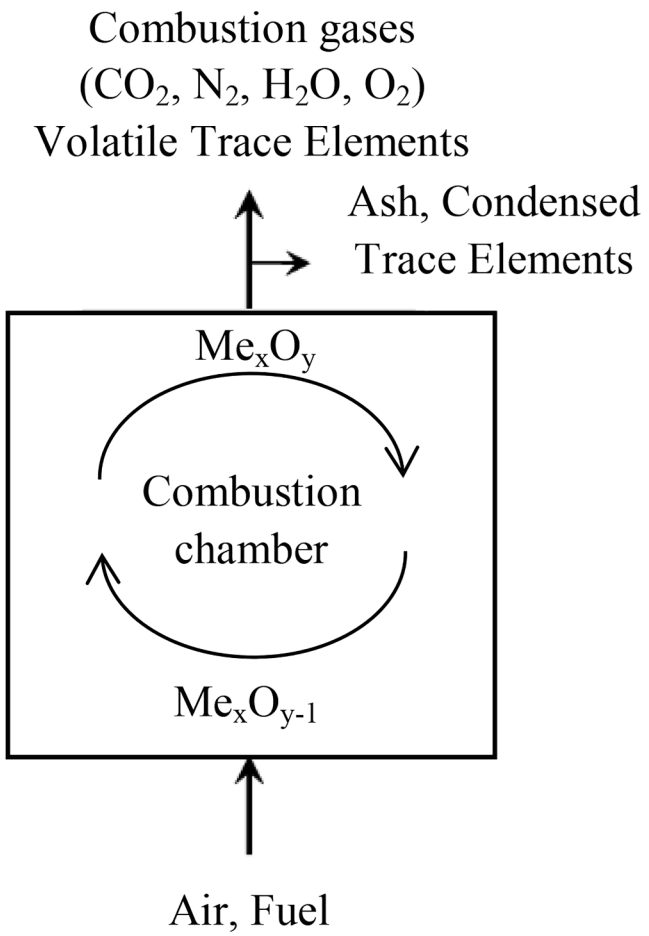

Fig. 1. Schematic description of Oxygen Carrier Aided Combustion (OCAC).

Research on the interaction between oxygen carriers and ash components has mainly focused on coal ashes, with most studies being conducted in bench-scale experiments, often related to CLC [21–26]. It has been reported that coal ash deposits on the surface of iron-based oxygen carriers form compounds with low melting temperatures, thus affecting the activity of the material [21]. Other findings relate a decrease in oxygen carrier reactivity to the presence of ash components, with the exception of ashes with high shares of Fe_2O_3 or $CaSO_4$, which can function as oxygen carriers themselves [21–23]. An increase of activity of ilmenite, the oxygen carrier in focus in this work, was reported due to interaction with alkali and alkaline earth metals [27]. Some studies have been conducted on the ash layer buildup and sulfur interaction when using ilmenite in OCAC-applications [28–30], mainly focusing on interactions with calcium and potassium. Calcium forms a double ash layer on the ilmenite particle with increased Fe content between the Ca layers [29,30]. With increasing residence time, potassium diffuses into the ilmenite particle core, forming titanates. Other observations relate to the segregation of iron to the surface and enrichment of titanium in the particle core [29–31]. Furthermore, magnetic separation of bed material effectively separates reactive material from low-quality oxygen carrier and inert material [31]. Increased porosity and ash layer formation can strengthen the material mechanically and does not directly inhibit the reactivity of the bed material. However, the buildup of thick layers of ash with increasing residence time could decrease the reactivity. Optimization measures have been suggested where activated material is separated by a magnet and reused in the system [31].

Studies have shown that the combustion of waste-derived fuels in fluidized bed boilers may increase trace elements in the fly ashes besides the common alkali and alkaline earth metal compounds [32]. One crucial parameter is chlorine which affects the volatilization behavior of the trace elements [32]. Since the affinity towards alkalis is higher compared to metals (H > K/Na > Pb > other heavy metals) alkalis will, in its turn, govern the availability of Cl [32]. When alkali and heavy metal chlorides form, they follow the flue gas into the convection path of the boiler, where they can cause corrosion and fouling [33]. It has been reported that heavy metal chlorides can induce corrosion at temperatures as low as 250-300 °C [34] and the formation and behavior of heavy metals are not yet as widely understood as alkali metals. The formation of gaseous alkali chlorides also promotes reaction with silicates due to increased mobility [35]. However, sulfur may decrease heavy metal volatility due to the formation of condensed sulfate phases. The influence of sulfur on the volatilization of heavy metals has been discussed in the literature [36–38]. For example, metal sulfates may remain stable even at high temperatures [38], and the release of heavy metals is sensitive to both Cl and S concentrations in the fuel.

Thermodynamic equilibrium calculations can be utilized in a wide range of applications. For example, to study ash characteristics [39], the interaction between oxygen carriers and ash components [40–43] or the behavior of trace elements [44–47]. Becidan et al. [46] studied separate waste fractions of MSW and their influence on the behavior of alkali metals and trace elements during combustion. The study found that when chlorine is available, sodium forms NaCl, suppressing the formation of metal chlorides. If most of the fuel consists of PVC (with a small amount of Na), metal chlorides will be the thermodynamically stable compounds. When the sulfur and chlorine fractions are low, metal oxides will form. Independent of the waste fuel which is combusted, Pb seemed to end up in the gas phase [46].

By investigating samples obtained from industrial applications that utilize complex waste fuels, unique and highly relevant information on the solid-state chemistry and the fate of important elements can be obtained. As described above, the investigations are limited and have focused mainly on impurities such as K, S and Ca, with no investigations of trace metals. Recently our group has studied the interactions of

ilmenite and the important trace elements Zn, Cu and Pb during OCAC combustion of MSW [48]. Here, a combination of detailed solid-state analysis of bed samples and thermodynamics was employed to better understand the trace elements. Copper and zinc ferrites and lead titanates were identified on ilmenite particle surfaces. This work aims to study a time series of solid industrial samples derived from OCAC of MSW using the oxygen carrier ilmenite. The objective is to reach an increased understanding of the behavior of trace elements, by determining the relationship between different parameters, the chemical speciation of the trace elements, and interaction with varying bed materials. More specifically, this investigation will:

- Study the influence of residence time on the interaction between the important trace elements Cu, Zn, Pb and Cr and the bed material: silica sand and ilmenite
- Investigate whether the magnetic separation of ashes affects the concentration of the trace elements.
- Analyze the particle interior with respect to trace element concentration and chemical speciation.
- Use thermodynamic equilibrium calculations to investigate the influence of temperature, reduction potential, chlorine, sulfur, and different bed materials.

This type of analysis of materials with different residence times will provide a deeper understanding of the critical transformations in the OCAC system concerning these metals.

2. Material and method

The samples in this study have been taken from the P14 boiler at Händelö, Sweden, a 75 MW_{th} CFB boiler that provides electricity and heat to the local district heating network. The boiler is owned by the company E.ON. Since November 2014, the boiler is being occasionally operated with ilmenite as bed material. The boiler is usually operated with a mixture of MSW and industrial waste but allows sewage sludge and rubber to be used. Further information can be found elsewhere [14,48,49]. In total 35 samples were collected, 20 bottom ash samples and 15 fly ash samples. During the 38-day period over which the samples were collected, the fuel consisted of municipal solid waste.

2.1. Sample selection

The bottom and fly ash samples investigated in this work have been collected over a period of 38 days, meaning that the bed material particles have a range of different residence times together with reactive ash components, amiable for solid-state characterization. The boiler was initially operated with silica sand as bed material. During the 38 days of sampling, ilmenite was fed to the boiler. In the furnace, fuel is fed in three different positions at the height of four meters. Bed material is fed on top of the fuel and enters the boiler together with it. Through ports located at the bottom of the furnace, coarse bed material and inert materials from the fuel (cables, metal parts, tiles, concrete, etc.) are continuously removed with the help of two water-cooled screw conveyors. After that, larger fractions are removed using a drum sieve while the finer fraction, suitable as bed material, is recirculated back to the furnace. During the 38 days, the outlet O_2-concentration varied between 5 and 8 vol% and the furnace temperature varied between 880 and 935 °C.

The bed material, fly ash, and flue gas enters one of the two available cyclones at the top of the furnace, separating the heavier particles, which then fall to the loop seals at the bottom of the cyclones. Tertiary superheaters cool the material before it is returned to the furnace. The flue gas and fly ash, which are not collected in the cyclone, continue through an empty duct where they are cooled from approximately 900 °C to 700 °C before reaching the superheater section and the economizer. The temperature is lowered to approximately 170 °C after the economizer and the flue gas and fly ash enter the flue gas cleaning system, the Novel Integrated Desulfurization (NID) reactor. The cleaning process involves the use of limestone and activated carbon and consists of a circulating system involving mixers, reactors, and textile filters. To begin with, activated carbon is injected into the stream, after which the flue gases and fly ash reach the textile filters, where the remaining particles are removed. The cleaned flue gas goes through emission control before it is guided out through the chimney. After the textile filters, the remaining fly ash is collected in the bottom and is either sent to a silo or recirculated. Before recirculation, the fly ash is mixed with lime and injected just before the addition of activated carbon. The fly ash was sampled after the addition of activated carbon and limestone before the textile filters. The sampled bottom ash was left to cool before sieving.

All sampled bottom ashes were sieved below <710 μm to remove larger pieces and magnetically separated two times to obtain an ilmenite-rich fraction (referred to as magnetic accept) and a silica sand-rich fraction (referred to as magnetic reject) [31]. The magnetic separation was performed using a conveyor belt stretched across two horizontal cylinders. One cylinder is connected to an electric motor while the other contains Rare Earth Roll (RER) magnets.

2.2. Characterization techniques

The total elemental composition of the samples was analyzed using ICP-SMFS according to the standards EN ISO 17294-2: 2016 and EPA-method 200.8: 1994. These characterizations were performed by the company ALS Scandinavia. Crystalline bulk phases were determined using powder X-ray diffraction (XRD) with $CuK_{\alpha 1}$ radiation in a Bruker D8 Advanced system. Bottom ash samples were lightly crushed in a mortar. Scans were made over a 2θ-range between 20° and 80° with a step size of 0.05° and counting time 2 s/step. The same settings (40 kV, 40 mA) were used for all samples.

The morphology was examined using Scanning Electron Microscopy (SEM). The microscope is coupled to an Energy Dispersive X-ray Spectroscopy (EDX), which allows the study of elemental distribution. The system used for this investigation was Quanta 200FEG coupled with an Oxford EDX system. For elemental distribution, both point- and elemental map analyses were used. Surface morphology and elemental composition were studied by mounting the particles on carbon tape. Samples were also prepared by molding particles in epoxy resin. Thereafter, samples were polished to study the interior of the particles.

X-ray Photoelectron Spectroscopy (XPS) provides both elemental and chemical state information of solid samples. One advantage with this method is the low detection limits which allow identification of elements down to 0.1 at%. The PHI 5000 VersaProbe III Scanning XPS Microprobe (Base pressure of 1×10^{-9} bar) has been used with monochromated Al-source (25 W). Dual beam charge neutralization was used for charge compensation during measurements. Spectra were recorded with a 100 μm beam size and pass energy of 224 eV for surveys and 26 eV for region spectra respectively, same settings as in a previous paper [48]. The survey spectra are used to quantify the surface composition while the region spectra, which record element-specific regions, are used for chemical state identification. Analysis points were chosen based on x-ray induced secondary electron imaging allowing to define analysis points with good accuracy. Survey analyses were performed on at least three particles per sample for both the cross-section and surface. The metal concentrations reported in this paper for both SEM-EDX and XPS are given in atomic percent. The given values are based on the ash elements and oxygen identified in each specific analysis.

Charge referencing was made to the adventitious C 1s line at 284.8 eV to calibrate the binding energies of the core level photoelectron lines from other elements. The peak areas of each element were normalized by the atomic sensitivity factors (ASF) provided by Multipak software in the quantitative analyses of the surface composition [50]. Selected region spectra were recorded covering $Pb4f_{7/2}$, $Cu2p_{3/2}$ and $Zn2p_{3/2}$ for

the quantification and chemical state identification [50,51]. The high-resolution spectra were fitted using the Multipak software with Smart background. Peak constraints regarding the area ratios and spin–orbit separation were defined as reported in the literature [50]. Details on the fitting procedure have been described in a previous paper [48].

2.3. Thermodynamic study

Global thermodynamic calculations were performed to investigate the influence of temperature, reduction potential and bed composition on trace element partitioning and phase distribution. In a previous paper, the phase distribution in an ilmenite-rich bed including MSW was presented over a range of reduction potential [48]. Some questions which arose in the previous paper relate to the influence of the bed material and the fuel composition. For example, during the calculation in the preceding paper, it was noted that MSW, which contains higher concentrations of Cl and S compared to recycled waste wood, influenced the partitioning of trace elements and gas-phase equilibrium. Therefore, the influence of fuel-bound sulfur and chlorine will be investigated in this paper along with the effect of temperature changes and bed material composition, i.e., a combination of ilmenite, silica sand, and ash.

The MSW composition used for the calculations in this paper was estimated using the average of six elemental analyses reported by Avfall Sverige [52] and has previously been used for thermodynamic calculations [48]. Due to the heterogeneous nature of the fuel, it is difficult to obtain a representative fuel analysis, and the composition used in this paper is based on an extensive study performed at the plant in question. A sensitivity analysis was made using the six different fuel compositions [52]. The results are presented in Supplementary Material, Figs. S1–S4. Regarding the high residence time of the particles in the boiler one may expect that the bed material is exposed to an average value of the fuel composition, although the fuel itself may vary over time. Therefore, using a mean value of the reported compositions is deemed reasonable to provide insight into the fate of the investigated trace elements in the boiler.

Four different cases, based on variation in bed material composition, were studied in this paper. These will use different bed materials, the MSW fuel composition reported in Table 1 and air as input. In the first case, no bed material is used to illustrate the effect of ash accumulation in the system and the impact of inherent ash components. The two following cases include a 1:1 wt ratio between the MSW ash and bed material, either silica sand or ilmenite. The last case will consist of a 2:1:1 wt ratio between MSW ash, silica sand and ilmenite. For the four cases presented above, the following parameters were investigated:

Temperature span between 700 °C and 1100 °C, with an increment of 100 °C. The temperature measurements in the fluidized bed and cyclone during OCAC varied between 850 and 950 °C.

Reduction potential between $\log_{10}[pCO/pCO_2]$ = -8 and 0.1. As there may be oxygen-deficient and oxygen-rich areas in the boiler, the reduction potential will be studied. Higher reduction potentials apply to areas concentrated in fuel or inside the bed material particles where oxygen availability is low. The oxygen concentration in the outlet from the boiler varies around five vol% which corresponds to a reduction potential $\log_{10}[pCO/pCO_2]$ around −8. The change in reduction potential was realized by varying the amount of air resulting in a reduction of the air-to-fuel ratio. The relation between oxygen partial pressure and reduction potential can be found elsewhere [48].

The sulfur and chlorine content in the fuel was varied to study the effect on trace element partitioning. Examples of MSW constituents that may affect this balance are batteries, food waste and PVC, which can contribute to enhanced Cl-concentrations while impregnated wood, gypsum and leather can contribute to the elevation of S [37,46,53]. The change was realized by increasing the amount of S or Cl in the fuel individually.

Thermodynamic calculations were performed using the software FactSage 7.2 [54]. The program consists of calculation and manipulation modules that access different solution databases and substances to calculate phase diagrams or conditions for multiphase, multicomponent equilibrium. In this study, the module *Equilib* was used. This module requires reactant inputs, temperature, total pressure, possible product phases and solution databases to be specified. The module employs the Gibbs energy minimization principle to calculate the amount of each product at the equilibrium state [54]. The thermodynamic databases used for this purpose were FactPS, FToxid, FTsalt and HSCA, previously used for the same purpose of global thermodynamic calculations [48]. The final calculations consisted of 1877 species (667 solids and 524 gases), 84 solutions and 752 phases. For this study, additional species were added originating from HSC Chemistry 10 [55], while the previous paper included data from HSC Chemistry 9. The compounds added for this paper include $CuAl_2O_4$, $Cu_2Al_2O_4$, $CuCr_2O_4$, Ca_2PbO_4, Cu_2PbO_2, $K_2Pb(SO_4)_2$, $Pb_3(AsO_4)_2$, PbS_2SiO_4, $PbSiO_4$, $Pb_5Si_3O_{11}$. The final calculations included 59 solid and 79 gaseous species from this database. The database comprises trace element compounds of As, Co, Cr, Cu, Mn, Mo, Ni, Pb, V and Zn. Hence, it is believed that the quality of the calculations is improved with respect to these species compared to the use of only the FACT databases.

Table 1
Fuel composition of Municipal Solid Waste (MSW). Daf: dry and ash free.

Species	Unit	MSW
Ash content	wt%	13.05
Moisture	wt%	37.1
C	wt% daf	58.4
H	wt% daf	7.6
S	wt% daf	0.8
N	wt% daf	1.4
Cl	wt% daf	1.0
Al	wt% ash	6.7
Ca	wt% ash	16.0
Fe	wt% ash	3.6
K	wt% ash	1.7
Mg	wt% ash	1.9
Na	wt% ash	3.6
Si	wt% ash	21.1
Ti	wt% ash	1.0
As	mg/kg ash	126
Ba	mg/kg ash	1479
Co	mg/kg ash	42
Cr	mg/kg ash	966
Cu	mg/kg ash	3871
Mo	mg/kg ash	48
Mn	mg/kg ash	1044
Ni	mg/kg ash	883
P	mg/kg ash	4437
Pb	mg/kg ash	3358
V	mg/kg ash	68
Zn	mg/kg ash	4280

3. Results

Before the ilmenite feeding started to the boiler, one bottom and one fly ash were sampled (Day 1.1) after which feeding of ilmenite started (0.8 kg/MWh). For the following four days, samples were regularly extracted. A summary of the collected samples is presented in Table 2. The table includes days with ilmenite operation, sample types and acronyms, along with the magnetic fraction obtained for each day. If several samples were extracted on the same day the samples are labeled as x.y (day x. sample y). Before the ilmenite feeding, the magnetic fraction was 9.6 wt%, and after 38 days of operation it increased to 41.6 wt%. On day 32, ilmenite feeding was increased to 3.0 kg/MWh. This change induced a rapid increase in the magnetic fraction, which became 44.7% at most. The residence time of the ilmenite particles has been estimated using the magnetic fraction and concentration of titanium in the magnetic bottom ash. The mean residence time is 29 h for the lower feeding rate (0.8 kg/MWh) and 24 h for the higher feeding rate (3 kg/

Table 2
Summary of collected samples, type of ash, day of sampling and corresponding magnetic fraction.

Day	Time of operation [h]	Ilmenite feeding [kg/MWh]	Sample type			Magnetic fraction in bottom ash [wt %]
			Fly ash	Bottom ash Magnetic Accept	Bottom ash Magnetic Reject	
1.1	–	Before ilmenite feeding	FA	BA-M	BA-R	9.6
2.1	19	0.8	FA	BA-M	BA-R	13.8
2.2	24	0.8	FA	BA-M		14.4
2.3	30	0.8	FA	BA-M		15.9
3.1	43	0.8	FA	BA-M	BA-R	16.3
3.2	49	0.8	FA	BA-M		15.8
3.3	54	0.8	FA	BA-M		16.7
4	67	0.8	FA	BA-M	BA-R	17.0
14	307	0.8		BA-M		24.7
21	475	0.8		BA-M		20.3
24	550	0.8		BA-M	BA-R	19.6
25	571	0.8	FA	BA-M		20.8
28	642	0.8	FA	BA-M		17.6
31	715	0.8	FA	BA-M		21.7
32.1	739	0.8	FA	BA-M		27.8
32.2	748	3.0	FA	BA-M		34.2
33	762	3.0	FA	BA-M		30.6
36	842	3.0	FA	BA-M		44.7
37	868	3.0	FA	BA-M		37.1
38	893	3.0	FA	BA-M		41.6

MWh). Considering a well-mixed solid phase and continual feeding and extraction (bottom bed and fly ash) of oxygen carrier during 893 h, it can be expected that particles will be extracted which can have spent hundreds of hours exposed to waste combustion.

The elemental composition of selected samples is presented in Table 3. The composition of fresh ilmenite is reported as received from the supplier. An increasing amount of Fe and Ti in the bed can be observed with time in the magnetic fraction. It is expected that most of the ilmenite will be found here, as ilmenite is known to be susceptible to magnetism [56]. Some noteworthy differences in composition can be observed in the table. For example, it is clear from the table that the fly ash is enriched in Ca, Na, K, Al, Pb, Cl and S. Pb is mainly concentrated in the fly ash and equally distributed between the magnetic rejected and accepted bottom ash fraction. The magnetic bottom ash fraction increases in Ca, Mg, Mn, Cr, Ni and Zn content over time relative to the magnetic reject fraction which is enriched in Si, Al, and K. Cu is slightly enriched in the fly ash. Comparing the Cu concentration in the two bottom ash fractions shows enrichment in the rejected magnetic bottom ash fraction during the first days. Over time, the magnetic fraction increases in copper concentration, resulting in a fairly equal distribution among the two bottom ash fractions.

3.1. Global thermodynamic equilibrium – bed material variation

3.1.1. Temperature variation

The influence of temperature is studied for different bed materials utilized in OCAC. Calculations were performed using a temperature interval between 700 and 1100 °C with an increment of 100 °C, the total pressure of 1 atm and five vol% O_2. The solid phase distribution with different bed materials is presented in Fig. 2. More than 50 wt% of the total phases are slag at temperatures above 850 °C when silica sand is used as bed material. The slag phase could imply operational difficulties such as defluidization due to agglomeration and sintering. For ilmenite, the slag forms at higher temperatures, and in a mixed bed, the slag phase is formed, but to a lower extent than with the silica sand bed. The major constituents in respective solid solutions are summarized in Table 4.

The slag phase could dissolve trace elements, thus preventing them from entering the gas phase. The major influence is observed for copper and lead. For example, below 850 °C, with minor slag phase, Fig. 3 shows that the silica sand bed yields over 70% copper chlorides in the gas phase while all other bed materials form ~10% copper chlorides with the rest being copper ferrites. Above 850 °C, for a silica sand bed and a mixed bed, the slag phase is observed to fixate both lead, Fig. 4, and copper, producing fewer metal chlorides. This could imply less

Table 3
Elemental composition of samples as provided by ALS Scandinavia and fresh ilmenite as provided by the supplier.

Sample		Fresh	BA M-1.1	BA M-2.1	BA M-4	BA M-24	BA M-32.1	BA M-36	BA M-38	FA 1.1	FA 2.2	FA 38	BA R-2.1	BA R-4	BA R-24
Element	Unit														
Fe	wt%	33.3	11.0	13.1	13.9	22.5	21.5	21.8	23.3	2.6	3.1	3.9	1.2	1.2	1.3
Ti	wt%	23.9	1.5	3.8	6.5	7.0	10.6	12.5	12.8	1.1	1.2	1.3	0.7	0.6	0.7
Ca	wt%	0.3	15.6	14.7	13.1	13.0	11.1	9.8	10.8	20.0	21.0	17.9	14.3	10.9	9.6
Si	wt%	0.9	16.6	14.6	15.4	8.6	9.6	7.7	7.4	8.0	8.9	8.8	29.1	28.5	31.9
Al	wt%	0.3	4.7	4.0	3.5	2.6	2.8	2.2	2.2	7.8	7.6	6.8	3.3	3.1	4.2
Mg	wt%	1.8	1.8	1.8	1.9	1.4	1.9	1.7	1.9	1.5	1.7	1.6	0.9	0.9	0.8
K	wt%	0.1	0.9	0.7	0.8	0.4	0.6	0.5	0.4	1.2	1.2	1.3	0.9	1.1	1.1
Na	wt%	0.1	2.0	1.9	1.8	1.0	1.5	1.2	1.1	2.1	2.2	2.1	1.4	1.6	1.6
Mn	wt%	0.1	0.2	0.2	0.2	0.3	0.3	0.3	0.3	0.1	0.1	0.1	0.1	0.1	0.1
P	wt%	–	0.4	0.3	0.3	0.2	0.3	0.3	0.3	0.4	0.5	0.4	0.3	0.2	0.2
S	wt%	–	2.7	1.9	1.4	1.3	1.0	0.5	1.4	3.8	3.9	2.6	2.7	1.6	0.7
Cr	mg/kg	–	2050	1650	1110	2590	1000	886	1040	439	466	480	382	294	299
Cu	mg/kg	100	2390	2040	2710	6310	3230	3360	5210	4430	4090	7090	4020	4270	6020
Ni	mg/kg	–	718	736	471	1290	689	462	464	209	203	234	62	79	79
Pb	mg/kg	<0.0001	530	549	868	716	582	587	668	2250	2280	2420	689	758	716
Zn	mg/kg	100	7050	6950	7560	12,700	9530	8260	11,200	6080	5920	8280	3340	3850	4280

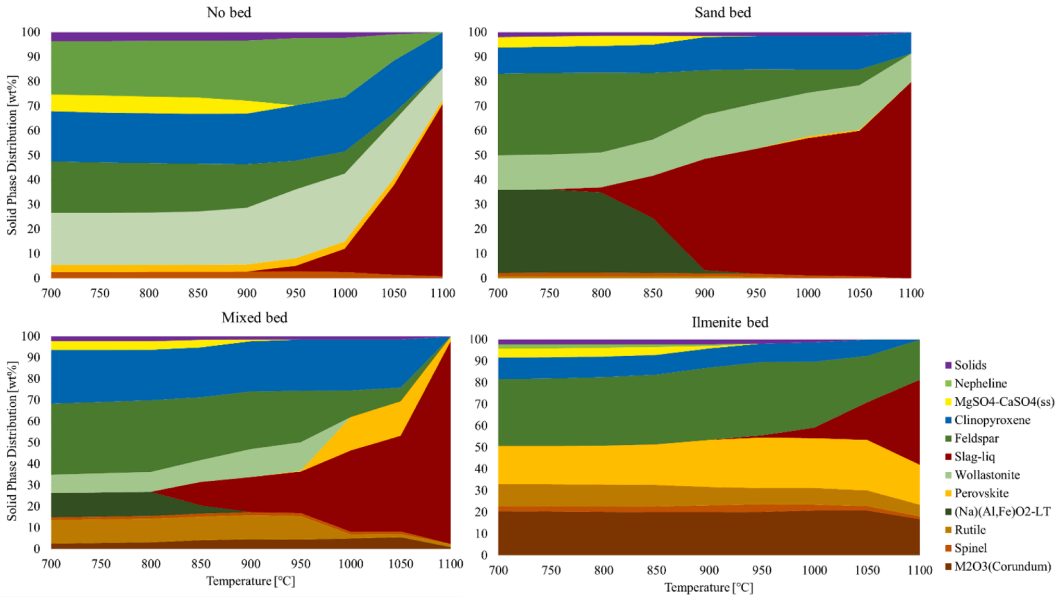

Fig. 2. Solid-phase distribution during combustion of MSW between 700 °C and 1100 °C and five vol% O_2 in the gas phase, as predicted by equilibrium calculations. Case with no bed material (upper left). Case with 1:1 wt ratio between MSW ash and: silica sand (upper right), ilmenite (lower right) and an equally mixed bed with silica sand and ilmenite (lower left).

Table 4
List over stable solid solutions and their major constituents for phase diagrams presented in this paper.

Phase	Major constituents
Nepheline	(Na,K)AlSiO4
MgSO4-CaSO4(ss)	$CaSO_4$
Clinopyroxene	(Ca,Fe,Mg)(Mg,Fe,Al)(Al,Fe,Si)SiO_6
Feldspar	(Na,K)$AlSi_3O_8$ - $CaAl_2Si_2O_8$
Slag-liq	SiO_2 + (Na,K)AlO_2 + (Na_2, K_2, Cu_2, Pb, Zn)O
Wollastonite	$CaSiO_3$
Perovskite	$CaTiO_3$
(Na)(Al,Fe)O2-LT	SiO_2
Rutile	TiO_2
Spinel	(Al,Co,Cr,Fe,Mg,Ni,Zn)$_3O_4$
M2O3 (Corundum)	(Fe,Al,Mn,Cr)$_2O_3$
Titania_Spinel	(Mg,Fe,Mn)(Mg,Fe,Mn,Ti,Al)$_2O_4$
Willemite	(Zn,Fe,Mg)$_2SiO_4$
Melilite	(Ca,Pb)$_2$(Zn,Fe,Si,Al)$_2O_7$

corrosion and prolonged life of heat exchanger surfaces. However, less metal chloride formation is accompanied by a higher amount of slag, which could result in agglomeration and in the worst case, defluidization of the bed. Fig. S5 in Supplementary Material shows that zinc is stable as $ZnFe_2O_4$ for all conditions with some dissolution in the slag phase with increasing temperature. The phase distribution of chromium, Fig. S6, is not affected by temperature variation and is distributed between Cr_2O_3 and (Fe, Zn)Cr_2O_4.

3.1.2. Variation in reduction potential

In a previous study, the influence of reduction potential was investigated thermodynamically, but only using ilmenite as bed material. Here, the reduction potential is studied for different bed material mixtures utilized in OCAC. The total pressure was specified to 1 atm and temperature set to 850 °C. The available oxygen was varied, resulting in different reduction potentials. The solid phase distribution with different bed materials is presented in Fig. S7 in Supplementary Material. Once again, a slag phase formation with the silica sand bed material can be observed with increasing reduction potential. For ilmenite, almost no slag phase is formed. Fig. 5 presents the trace element distribution in a mixed bed. The trace element distribution for no bed, silica sand bed and ilmenite bed are gathered in Fig. S8–S11 in Supplementary Material.

Following previous findings, the primary Cu phase is Cu ferrite during oxidizing conditions using ilmenite [48]. In an ilmenite bed and no bed, a mixture of Cu ferrites and chlorides form. The ferrite is reduced to Cu(s) with increasing reduction potential before entering the slag phase. With a silica sand bed, Cu is dissolved in the slag phase immediately, and in a mixed bed, Cu is mainly found in the slag phase throughout the whole interval of reduction potentials except for oxidizing conditions, where 30% of the Cu forms ferrites as observed in Fig. 5.

Pb is predominantly found in the gas phase as Pb chloride in an ilmenite bed or no bed. Increasing the reduction potential results in PbS (g) and Pb (g) formation for all cases. Adding a certain amount of silica sand shows positive effects on the Pb retention where over 60% is dissolved in the slag phase for a mixed bed, see Fig. 5, and silica sand bed up to the reduction potential −3.9, after which it enters the gas phase. There are no significant differences in the elemental content of Pb between the magnetic accept and reject fraction, according to Table 3. This suggests that Pb likely interacts with the particles regardless of the type of bed material used. Important to note is that when the HSCA-component $PbSiO_4$ was included, it was widely predicted. Due to constraints in thermodynamic data, where the component is valid up to 398 K, $PbSiO_4$ was removed from the calculations.

The inherent content of metals in MSW retains Zn and Cr in the bottom ashes in a spinel phase, Zn(Fe, Cr, Ni)$_2O_4$. The spinel phase is stable over a wide range with increasing concentrations of Zn(Cr, Ni)$_2O_4$ with higher reduction potential. In a mixed and sand bed, willemite (Zn, Fe)$_2SiO_4$ forms between the reduction potential −3.9 and −1.9 as previously reported [48]. Some Zn is also dissolved in a slag phase, but most is released as gaseous Zn under highly reducing conditions, observed in Fig. 5. Chromium forms Cr_2O_3 in ilmenite and mixed bed under oxidizing conditions, but when the reduction potential increases, Cr enters the spinel phase Cr(Fe, Zn, Ni)$_2O_4$ where it is kept stable.

3.1.3. Influence of variation in sulfur and chlorine concentrations

An increasing amount of S in the fuel increases the amount of SO_2 in the gas phase along with $CaSO_4$ in the solid phase, which has oxygen-carrying capabilities itself [21]. $CaSO_4$ increases on behalf of calcium silicates ($CaSiO_3$ and $CaMgSi_2O_6$). Since Ca and Mg silicates increase the

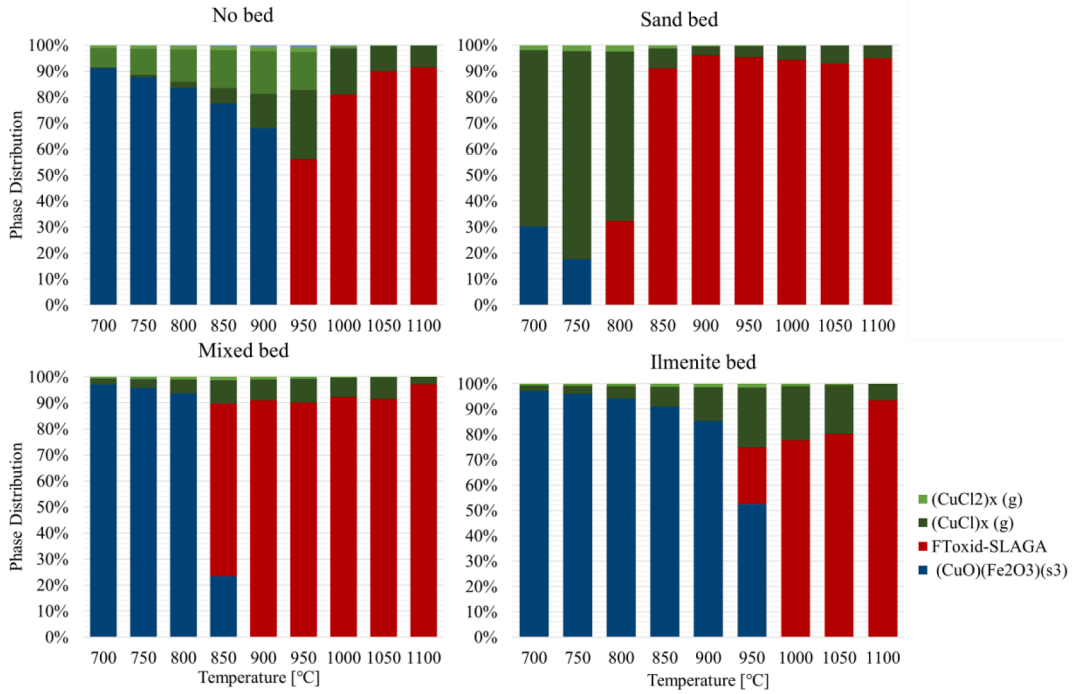

Fig. 3. Equilibrium copper phase distribution during combustion of MSW between 700 °C and 1100 °C and five vol% O_2 in the gas phase. Case with no bed material (upper left). Case with 1:1 wt ratio between MSW ash and: silica sand (upper right), ilmenite (lower right) and an equally mixed bed with silica sand and ilmenite (lower left).

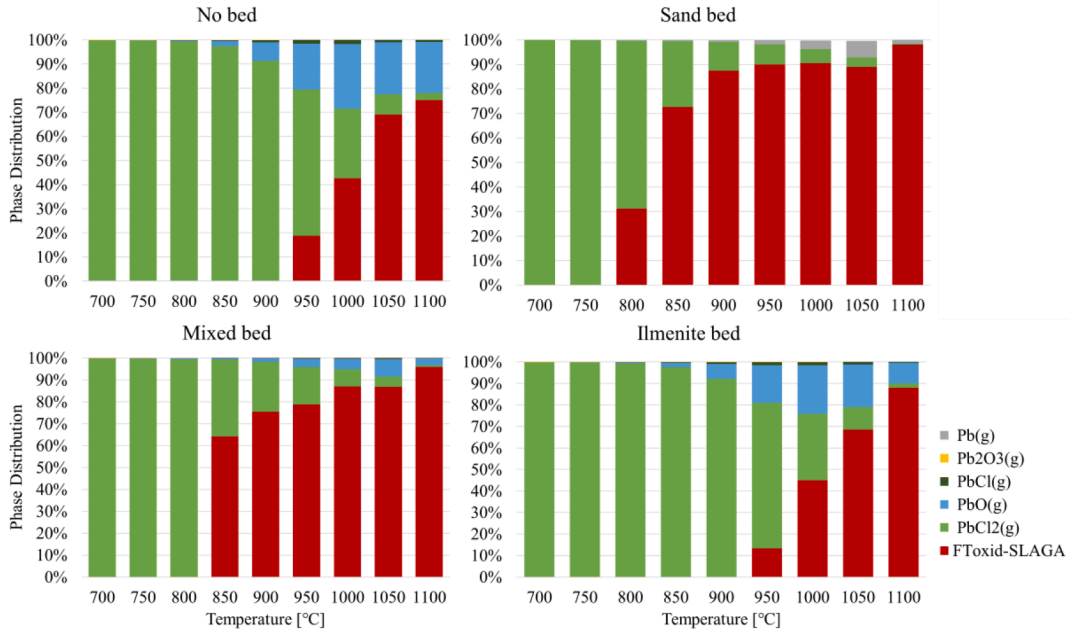

Fig. 4. Equilibrium lead phase distribution during combustion of MSW between 700 °C and 1100 °C and five vol% O_2 in the gas phase. Case with no bed material (upper left). Case with 1:1 wt ratio between MSW ash and: silica sand (upper right), ilmenite (lower right) and an equally mixed bed with silica sand and ilmenite (lower left).

melting point of silicate mixtures [57], the increased sulfur will increase the slag phase formation. The solid phase distribution for each bed material with varying S and Cl content is presented in Fig. S12 in the Supplementary Material. With increasing S, Cu and Pb are absorbed in a slag phase for all investigated bed materials. Over 90% of the Cu is retained as copper ferrite (ilmenite bed or no bed) or in a slag phase (silica sand bed and mixed bed) with higher S-contents. With more than 8.5 wt% daf sulfur in the fuel, fewer Pb chlorides form for all bed materials. Instead, Pb is partially dissolved in a slag phase. Adding S could prevent heavy metals from entering the gas phase, which could be beneficial, especially for an ilmenite bed where around 50% of Pb is associated with the melt, which only occupies about five wt% of the total phases.

An increasing amount of Cl slightly decreases the amount of slag and increases the HCl concentration in the gas phase along with some metal chlorides, mainly $PbCl_2$ and $(CuCl)_x$. The Cl-concentration clearly affects

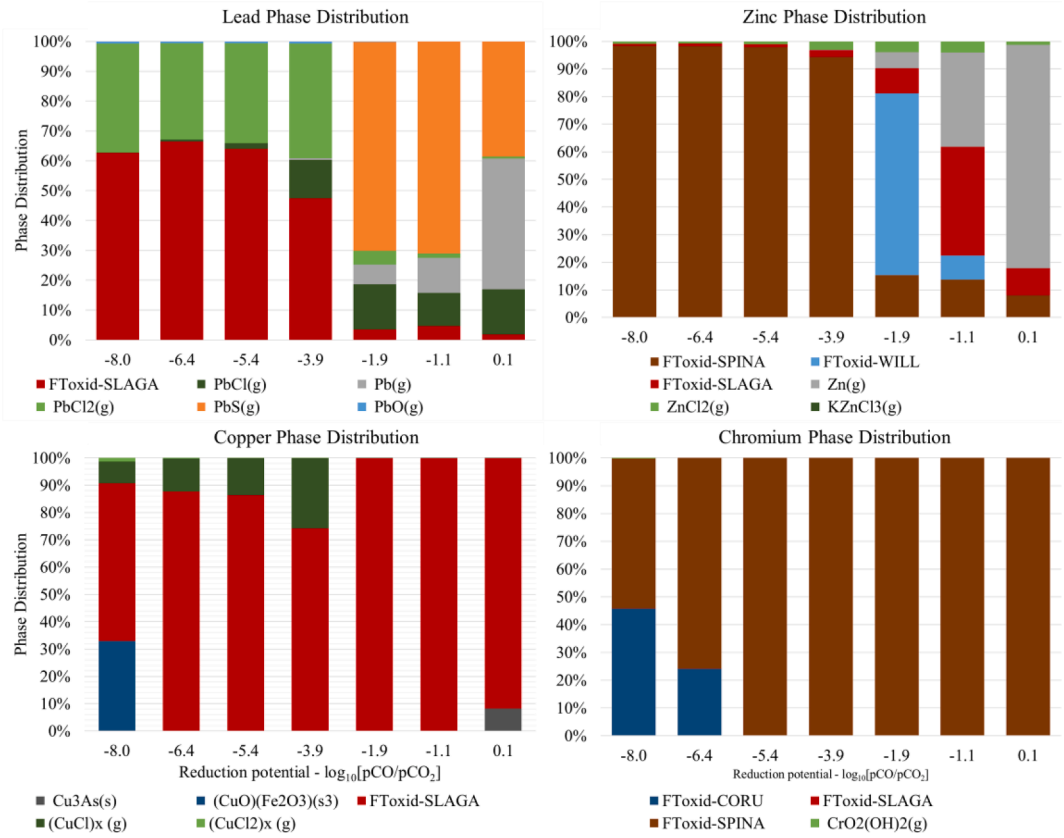

Fig. 5. Phase distribution of lead (upper left), zinc (upper right), copper (lower left) and chromium (lower right) in a mixed bed at 850 °C and increasing reduction potential.

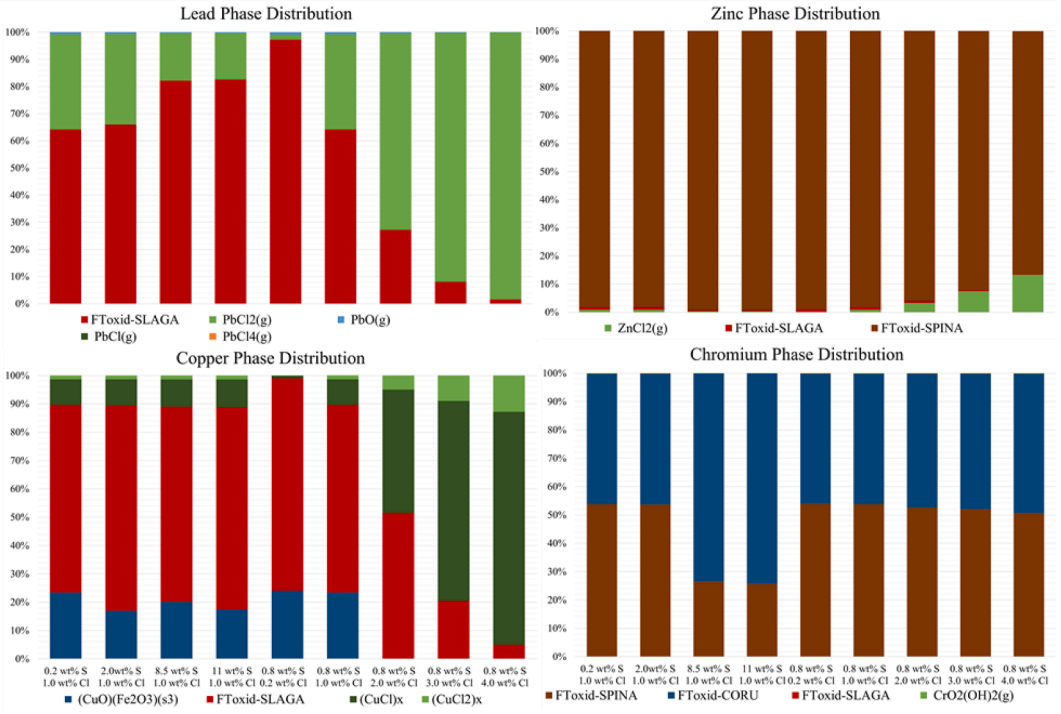

Fig. 6. Phase distribution of lead (upper left), zinc (upper right), copper (lower left) and chromium (lower right). Combustion in a mixed bed with variation in fuel in S and Cl composition at 850 °C and 0.05 atm O_2 over different S and Cl content ranges. Concentrations reported as wt% dry ash free.

the metal volatility. The trace element phase distribution in a mixed bed is presented in Fig. 6. Results for other bed materials are shown in Figs. S13–S15 in Supplementary Material. When the chlorine concentration increases to 4.0 wt% daf, the amount of gaseous Pb and Cu chlorides increase drastically to 95 and 98.4 %, respectively. Zn shows only a slight increase in volatility due to Cl-addition (maximum value of 13.4%) while Cr is stable as corundum Cr_2O_3 or in a spinel phase Cr(Fe, Zn, Ni)$_2O_4$ in all cases. The formation of gaseous metal chlorides increases their mobility which could aid the interaction with the bed material by sticking to the surface or diffusing through pores and cracks of the particles. To summarize, higher S concentrations in the fuel could lower the number of metal chlorides, but the Cl content has a more pronounced effect on the trace element distribution.

3.2. Bottom ash morphology and phase characterization

The major phase constituent in the 1.1 BA-R sample is SiO_2, followed by alkali and calcium silicates, as determined by XRD. In the corresponding magnetic fraction 1.1 BA-M some SiO_2 is present but along with aluminosilicates ((K,Na)$AlSi_3O_8$, $NaAlSi_2O_6$, (Ca_xNa_{2-x})($Mg_yFe_zAl_{1-y-z}$)Si_2O_7), $CaSiO_3$, $CaSO_4$ and some mixed iron oxides ($Mg_{1-x}Zn_xFe_2O_4$). It should be noted that although several crystalline compounds have been identified, the diffractograms also showed peaks which could not be correlated to a specific compound. The following days the amount of SiO_2 decreased in the bed, and other phases became more dominant. For example, peaks related to the ilmenite bed material Fe_2TiO_5 and Ca($Ti_{0.75}Fe_{0.25}$)O_3 phases were identified. These phases were confirmed in samples 24 BA-M and 38 BA-M. Furthermore, mixed iron oxides ($Mg_{1-x}Zn_xFe_2O_4$), aluminosilicates ((K,Na)$AlSi_3O_8$, (Ca_xNa_{2-x})($Mg_yFe_zAl_{1-y-z}$)Si_2O_7) and $CaSO_4$ were detected in all magnetic fractions. Phase characterization of sample 24 BA-R showed that the major difference between the phases is the more intense peaks of SiO_2 and alkali silicates in BA-R and mixed iron oxides in BA-M.

The crystalline phases are in large consistent with those predicted by thermodynamics in Fig. 2. The major difference is the amount of $CaSO_4$, which is predicted to be <5 wt%, while the diffractograms (and SEM micrographs below) indicate that the amount could be higher. Phases in the magnetic reject-fraction may be attributed to the case with silica sand, while the magnetic accept fraction has properties more like the case with an ilmenite bed as expected. A micrograph with an overview of the cross-section of particles can be observed in Fig. 7. Brighter spots indicate ilmenite particles, which increase in the magnetic bottom ash fraction over time.

Ilmenite particles exposed in the boiler for a longer period increase in size due to ash layer buildup and therefore contain other chemical elements besides Fe and Ti. Crack formation and increase in porosity also indicate the particle age. Based on these criteria, particles were selected and analyzed in the following sections. Chemical mappings were first performed on large areas and then specific particles to investigate the trace element distribution. Point analyses were used to verify the content of the trace elements which were observed in the mappings. A summary of micrographs of the bottom ashes over the period of 38 days is presented in Fig. 8, along with chemical mappings of Zn and Cu and the major components Fe and Ti for the magnetic fraction or Si for the magnetic reject fraction. These micrographs will be discussed further below for each trace element.

3.2.1. Fate of zinc

Low Zn concentrations can be observed on the outer parts of both sand and ilmenite particles for the first days. The micrograph, chemical mappings and point analyses of particles of 2.1 BA-M from Fig. 8 are presented in Fig. S16 in Supplementary Material. The micrograph shows one silica sand and one ilmenite particle obtained after one day of ilmenite feeding. An ash layer can be observed on both particles. The major ash components Ca, S, Mg, P and Na are observed on the surface of ilmenite. Zn seems to be concentrated in the outer ash layer of both particles with an enhanced intensity of Fe. Point analysis reveals a content of 1.3 at% Zn in this small section of the Fe-rich ash layer.

The Zn-concentration in ilmenite particles is enhanced at the surfaces and near cracks where oxygen availability is high. This can also be observed for the particle in samples 3.1 BA-M and 4 BA-M in Fig. 8. A line scan was performed on the ash layer of an ilmenite particle from sample 3.1 BA-M. Fig. 9 presents the chemical mappings and the Fe, Ti, Ca, Si and Zn variation over the layer. The formation of a double Ca layer

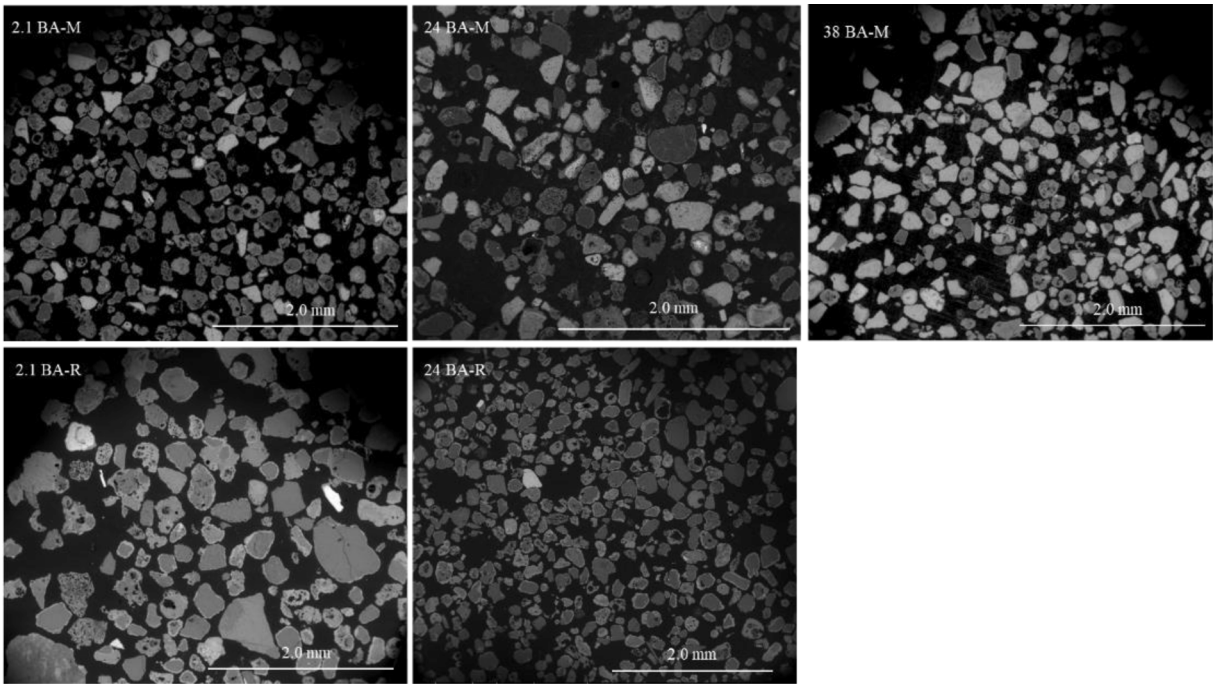

Fig. 7. SEM micrographs of the cross-section of bottom ash fractions magnetic accept and reject (BA-M and BA-R) for days 2, 24 and 38 with ilmenite operation. Images are obtained with BSE-detector, 20 kV.

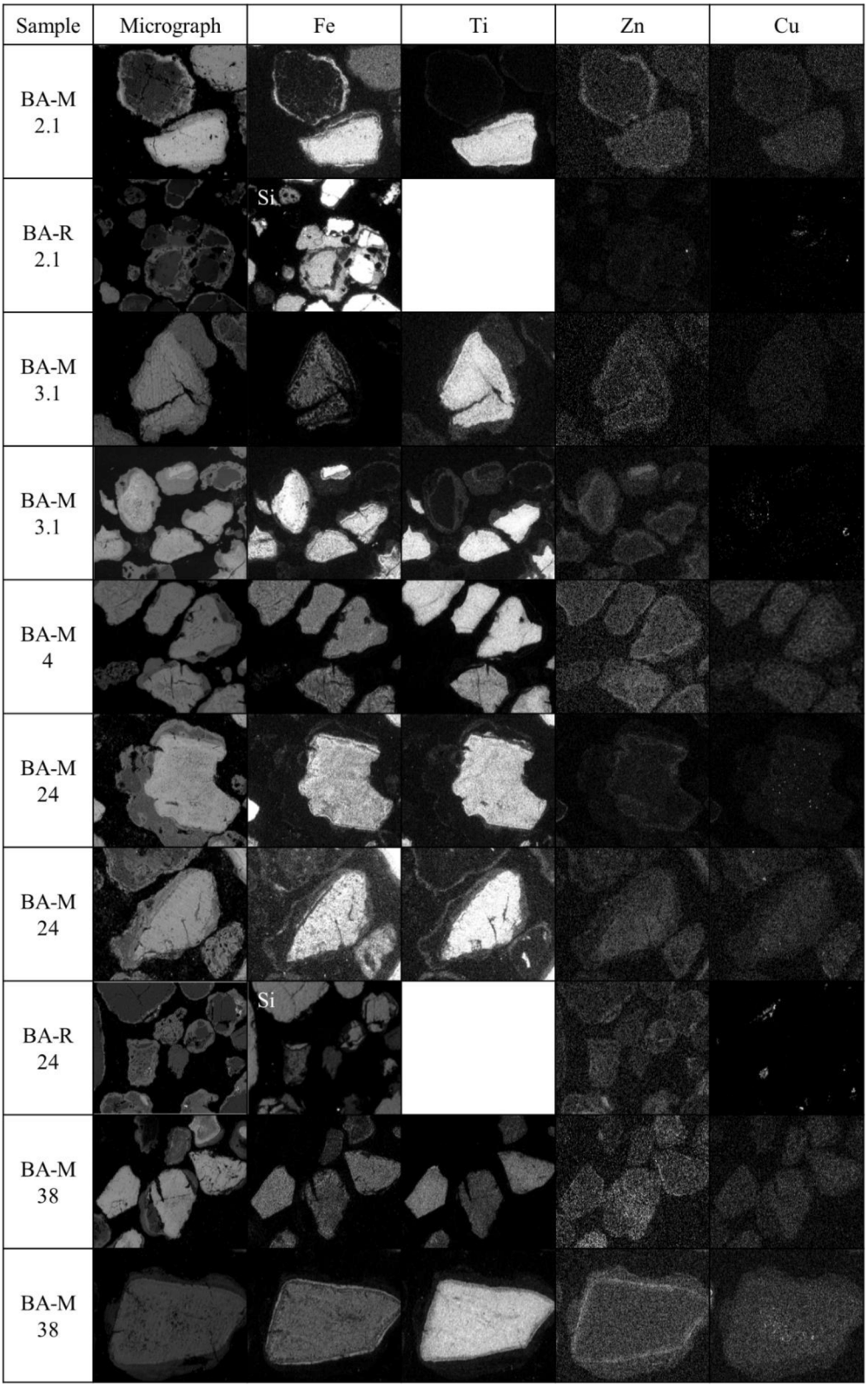

Fig. 8. A summary of SEM micrographs over the cross-section of particles obtained over a period of 38 days. SEM-EDX intensity maps for Cu and Zn with the major components' Fe and Ti for the magnetic fraction and Si for the magnetic reject fraction.

can be observed, as previously described in the literature [29]. In contrast to previous studies, the high S content in MSW has induced a thick outer layer covered with Ca. Furthermore, it is observed that Zn is enriched in the Fe layer formed between the two Ca layers. The Zn content in the inner layer increases with time. For day 38, the Zn-concentration is 2.1 at% in this Fe-rich ash layer. Point analyses of particle interior did not show enrichment of zinc. In the magnetic reject fraction, enhanced Zn-concentrations can be observed in the melt surrounding silica sand particles with higher K, Na, Ca and Si-contents (Fig. S17) or Fe (Fig. S18).

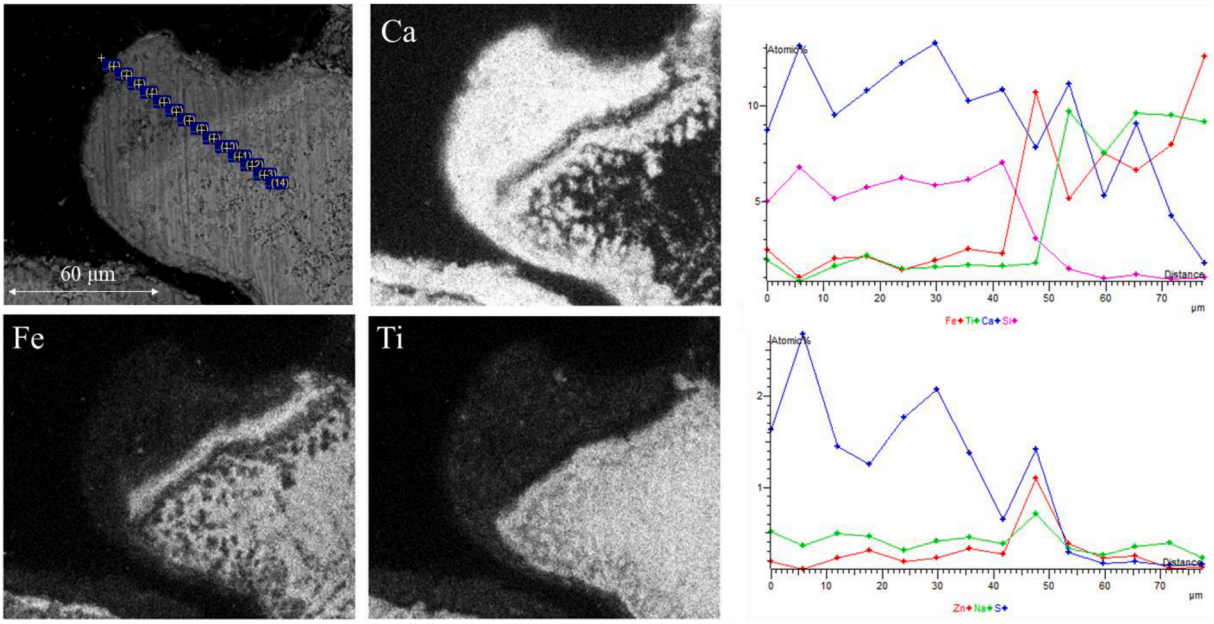

Fig. 9. SEM micrograph of the cross-section of sample 3.1 BA-M with corresponding EDX intensity maps showing the elemental distribution. Chemical composition, in atomic percent, over the ash layer acquired with line scan.

3.2.1.1. Detailed chemical speciation. To further investigate the trace element behavior, samples were studied using XPS. Both the surface and the cross-section of oxygen carrier particles were analyzed using XPS. To the best of our knowledge, this is the first such study reported concerning oxygen carrier particles with trace elements. The samples BA-M 1.1, 2.1, 14, 25 and 38 were studied to investigate the change of surface composition over time. Samples were chosen based on low (2.1 BA-M) and high (38 BA-M) residence times in the boiler. With increasing residence time, the particles are exposed to an increasing amount of ash and trace elements. Accumulation, if any, of the trace elements should thus be observable. Comparison between the samples may also provide insights regarding changes in chemical speciation over time. The change in Zn and Cu composition at the surface (hollow squares) and cross-section (solid circles) of particles are presented in Fig. 10.

Zinc concentrations on the particle surfaces were detected up to 0.72 at%, while the mean value lies in the range of 0.33–0.46 at% across the whole time interval. Binding energies obtained from region spectra are presented in Table 5. Values at ~1021.6 eV represent $ZnFe_2O_4$, while compounds at higher binding energies ~1022.4 eV are associated with either $ZnAl_2O_4$ or zinc silicates depending on the surface composition [48]. Small shifts in binding energy for $ZnFe_2O_4$ may be observed in Table 5. Slight deviations from stoichiometric compounds could result in a shift of the binding energy. When Zn ions replace Fe ions, the number of broken bonds may increase, resulting in a change in binding energy [58]. Concerning the cross-section XPS analysis, two values were detected slightly above 0.4 at%. These signals are attributed to the compound $ZnFe_2O_4$, which can be observed in the surrounding ash layer (see Fig. 9). Based on the elemental mapping previously presented in Fig. 9 and the concentration and chemical speciation, the signals likely originate from the ash layer.

3.2.2. Fate of copper

Cu shows a more extensive spread of surface concentration with time compared to Zn. The mean surface concentration lies in the range of 0.47–0.73 at% and seems to increase over time. Looking at the cross-section, the concentration increases from day 2 to 38, indicating accumulation of Cu, Fig. 10. No distinct enrichment of Cu can be observed inside the ilmenite particles during the first three days with ilmenite feeding, Figs. 8 and 10. However, with time enhanced Cu intensity is observed in the particle cross-sections. Fig. 11 presents an SEM-EDX analysis of a particle obtained from 38-BAM. Intensity maps are shown in the figure along with point analyses performed in the outer Ca ash layer (point 1), inner Fe ash layer (point 2) and inside the particle (point 3). Point analyses reveal that the copper concentration is 0.4 at% inside the particle. The increased penetration of Cu has been observed on a significant number of particles.

Studying the cross-section of magnetic reject bottom ash using SEM-EDX shows Cu inside the melt surrounding the sand particles, see 2.1 BA-R in Fig. 8. The same can be observed in the electron image of 4 BA-R presented in Fig. S17. Surrounding the sand particle is a molten slag phase that has caused the agglomeration of two particles in the upper right corner. Inside this melt, enhanced Cu concentrations are observed along with Al. Chemical mapping of the cross-section of 24 BA-R, Fig S18 in Supplementary Material, showed several bright spots in the melt surrounding the particles, which are linked to enhanced Cu, Cr and Pb concentrations. Cu is observed in the magnetic reject fraction, in surface micrographs of 24 BA-R along with Al or Fe, presented in Fig S19 in Supplementary Material.

3.2.2.1. Detailed chemical speciation. XPS identified two main surface components; $CuFe_2O_4$ at ~933.2 eV and Cu_2O, possibly combined with iron as $Cu_2Fe_2O_4$, located at ~932.8 eV. Table 5 shows the binding energies of the points presented in Fig. 10. Region spectra of the ilmenite cross-section revealed Cu^+, which is most likely in the form of $Cu_2Fe_2O_4$. A detailed SEM-EDX chemical mapping of the 24 BA-M particle cross-section is presented in Fig. 12. One can observe the coexistence of Ca and Ti while Fe is enhanced in small cracks and pores. Cu is observed to be concentrated in the vicinity of these Fe-rich areas. The oxygen availability may be lower inside the particles, and according to Fig. S8 in Supplementary Material, higher reduction potentials favor $Cu_2Fe_2O_4$ formation.

3.2.3. Fate of other trace elements

Pb was more difficult to observe with SEM in the bottom ash fractions due to low concentrations. However, XPS identified the Pb surface content <0.1 at%. The binding energies and corresponding Pb compounds are presented in Table 5. Pb silicates have been reported at 138.8 eV, Pb chlorides at 139.1 eV and Pb titanates at 137.9 eV. Detailed

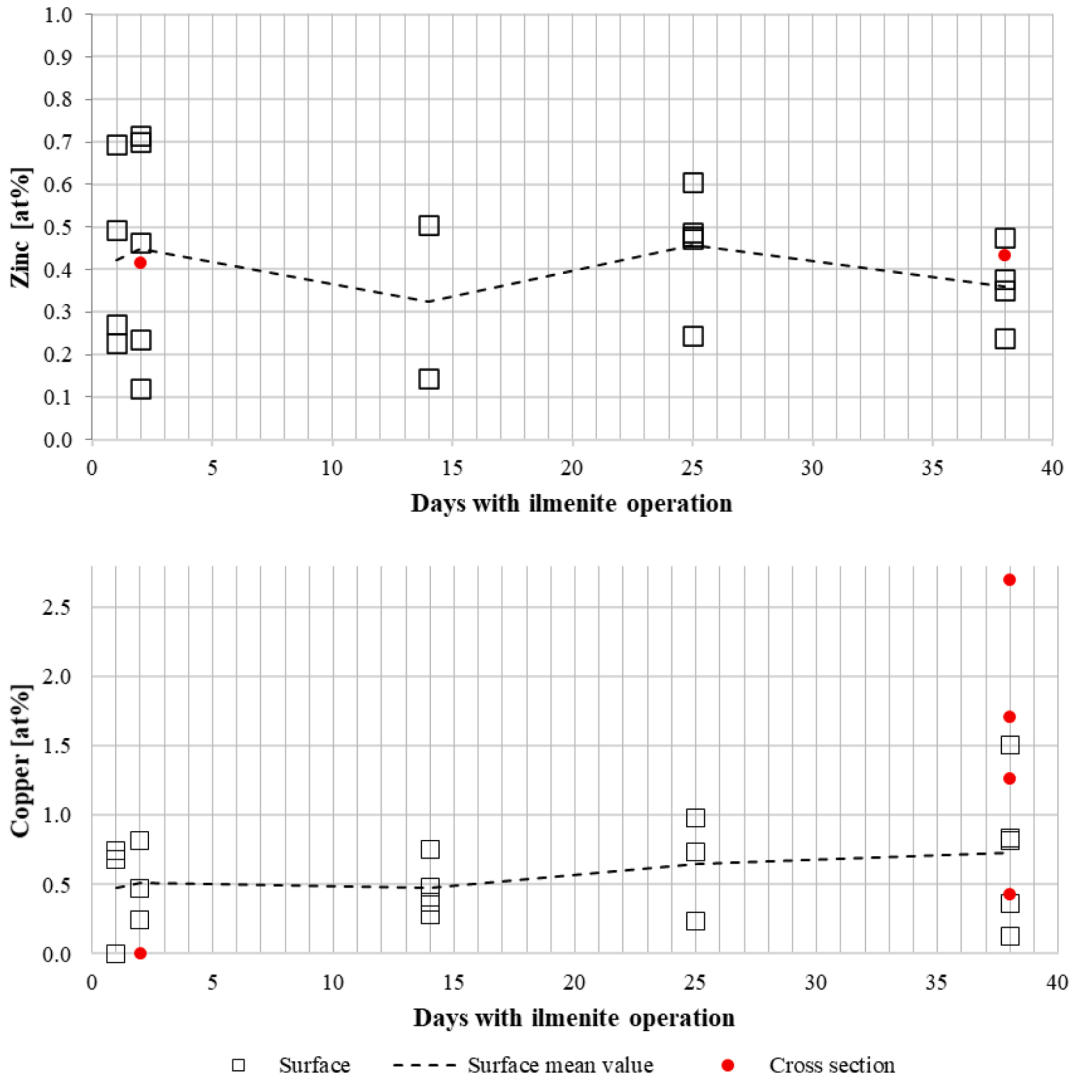

Fig. 10. The atomic concentrations (at%) of zinc (top figure) and copper (lower figure) over time as determined by XPS analysis. Hollow squares indicate values on the particle surface, and solid circles indicate interior values. The dashed line presents the mean value of the surface concentrations.

Table 5
Summary of the binding energy positions of the suggested components obtained from XPS region spectra analysis. *denotes positions with only one available data point.

Element	Position		BA-M				
			1.2	2.1	14	25	38
Zinc	Surface	$ZnFe_2O_4$	1021.3 ± 0.6	1021.4 ± 0.4	1021.6 ± 0.4	1021.2 ± 0.5	1021.3 ± 0.3
		$ZnAl_2O_4$/Zn-silicate	1022.2*		1022.4*	1022.4*	1022.4*
	Cross-section	$ZnFe_2O_4$		1021.4*			1021.5*
Copper	Surface	$CuFe_2O_4$	933.1 ± 0.2	933.2 ± 0.2	933.2 ± 0	933.2 ± 0.1	932.7 ± 0.4
	Cross-section	$Cu_2Fe_2O_4$		–			932.9 ± 0.3
Lead	Surface	$PbCl_2$	139.2 ± 0.3			139*	
		Pb-silicate		138.5*	138.8*		138.4*
	Cross-section	Pb-titanate		137.8*			137.8*

information on the fitting procedure can be found in the previous paper [48]. Both Pb chlorides and Pb silicates were observed on the particle surfaces. This could be due to sticky compounds found on the particle surface, for example, Fig. S18 in Supplementary Material where Pb-rich areas were detected surrounded by a melt. Pb was also detected in the particle interior by XPS, and the corresponding binding energy is well aligned with Pb titanate, although the concentrations were low <0.1 at %.

From the cross-section study, the particle interior did not show an increase in Cr concentration. Point analysis showed almost no Cr-content. However, Cr was detected with SEM on the particle surfaces. For example, in Fig. S20 in Supplementary Material, a spot with enhanced Ni-Cr-Fe-concentrations can be observed. Based on thermodynamic calculations, the most favorable compounds are Cr oxides. Chromium oxides have magnetic properties, allowing the particles to be magnetically separated. This is most likely the reason that Cr is enriched

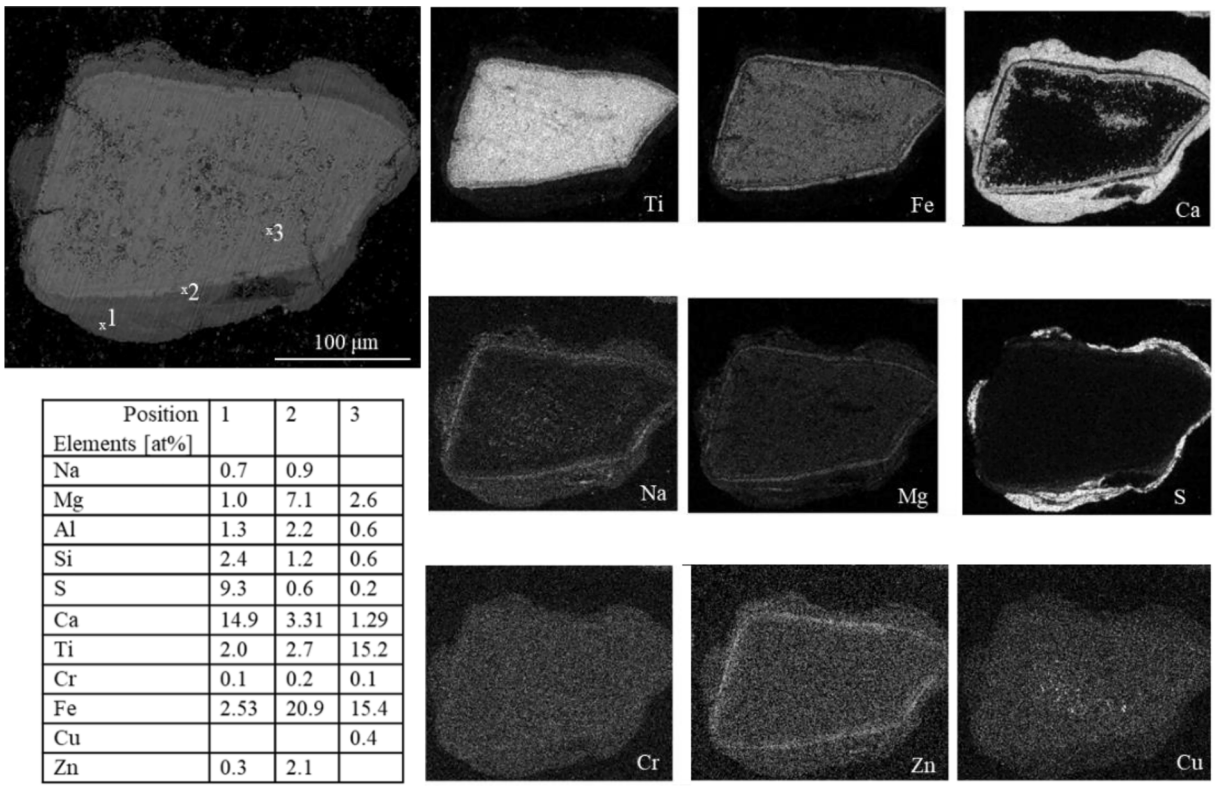

Position / Elements [at%]	1	2	3
Na	0.7	0.9	
Mg	1.0	7.1	2.6
Al	1.3	2.2	0.6
Si	2.4	1.2	0.6
S	9.3	0.6	0.2
Ca	14.9	3.31	1.29
Ti	2.0	2.7	15.2
Cr	0.1	0.2	0.1
Fe	2.53	20.9	15.4
Cu			0.4
Zn	0.3	2.1	

Fig. 11. SEM micrograph of the cross-section of sample 38 BA-M with corresponding EDX intensity maps showing the elemental distribution. Chemical composition, in atomic percent, acquired with point analyses.

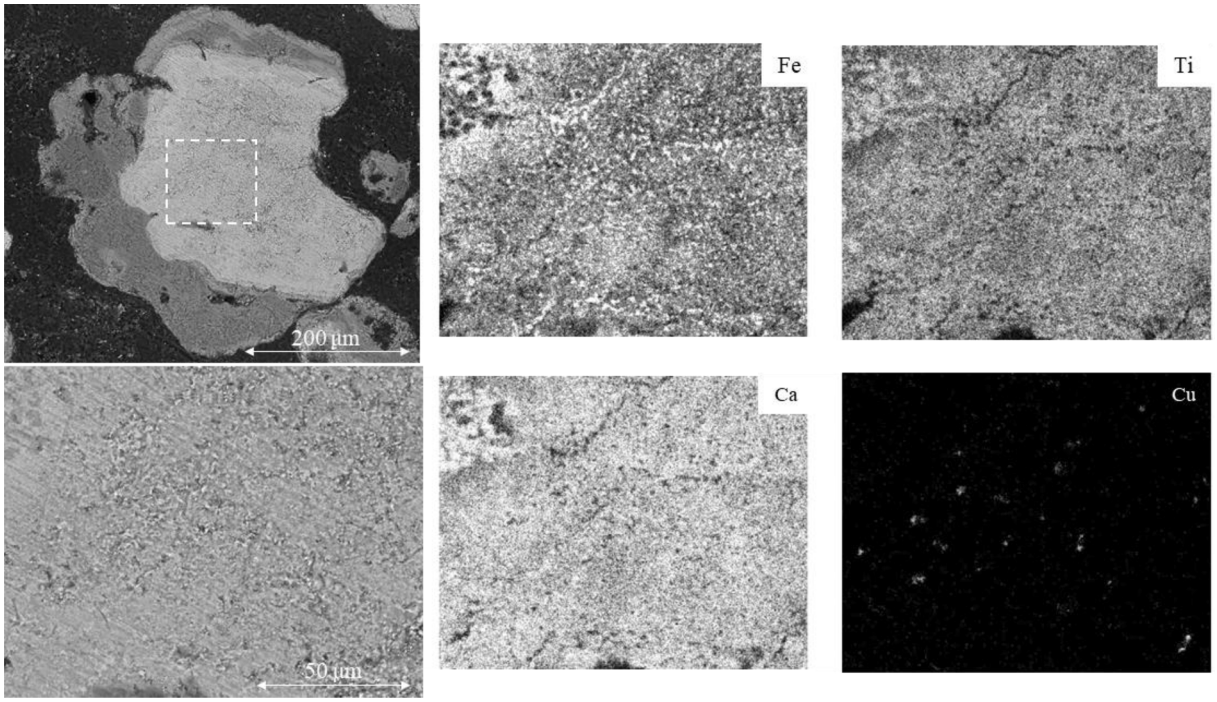

Fig. 12. SEM micrograph of the cross-section of sample 24 BA-M along with EDX intensity maps of Fe, Ti, Ca and Cu.

in the magnetic bottom ash fraction, see Table 3.

3.3. Fly ash morphology and phase characterization

Phase characterization of the fly ash showed that it consists of calcium sulfate and carbonate, aluminosilicates, quartz, metallic aluminum, and alkali chlorides. The major phase components, and the composition in Table 3, remain similar for 2.1 FA and 38 FA. One can observe that after 38 days, the S and Al concentrations slightly decrease while Fe increases along with Cu and Zn. The mapping of 38 FA

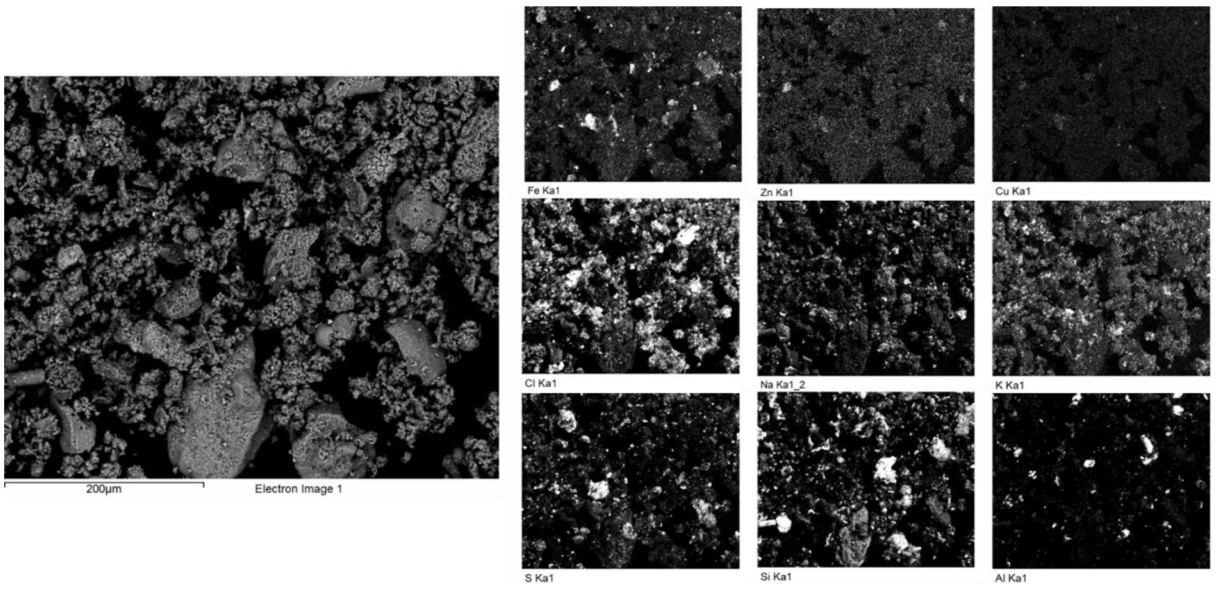

Fig. 13. SEM micrograph of the sample 38 FA along with EDX intensity maps of Fe, Zn, Cu, Cl, Na, K, S, Si and Al.

presented in Fig. 13 shows enhanced intensities of Cu and Zn along with Fe. More prominent bright spots of Cu and Zn may be correlated to enhanced Al or Fe concentrations, while minor spots correlate with higher Cl concentrations. XPS region measurements were performed on the samples 1.1 FA and 38 FA. The chemical speciation of the trace elements did not change with time. Data revealed two Zn components to be present, similar to the surface Zn in Table 5. These may be attributed to Zn ferrites and aluminates, also evident from the elemental mapping in Fig. 13. The presence of Cu ferrites was also confirmed. The content of Pb was observed in the fly ash at the binding energy 139.1 eV corresponding to lead chloride. Similar observations have previously been reported [48].

4. Discussion

This paper has studied the elements Cu, Pb, Cr and Zn in Oxygen Carrier Aided Combustion using ilmenite as an oxygen carrier. The influence of different bed materials, temperature, reduction potential, residence time and fuel composition has been investigated using a combinatorial theoretical and experimental approach. While the preceding paper [48] focused on surface speciation for one sample, this study has elaborated on the trace element distribution throughout the particle cross-section, evaluated during a longer time series spanning 893 h with continuous ilmenite addition.

It is clear from this study that the trace element chemistry is complex in OCAC and that the oxygen carrier can have significant effects. By magnetically separating the bottom ash, it is possible to obtain an ilmenite-rich fraction. With increasing operating time, the concentration of Zn, Cr and Cu will increase in the magnetic separated bottom ashes. The studied trace elements behave differently, with some more affected by oxygen carriers than others. For example, it is observed in Table 3 that Zn becomes enriched in the magnetic bottom ash in comparison to the fly ash and magnetic reject ash, with increasing time of ilmenite operation. This can be attributed to the fact that Zn ferrites are enriched in between the double Ca-layer. According to thermodynamic calculations, Zn is not as easily volatilized with increasing Cl-concentrations compared to Cu and Pb.

The Cu concentration is also observed to increase in the magnetic accept bottom ash relative to the magnetic reject ash, although the mechanism differs. The enrichment could be attributed to the accumulation inside ilmenite particles, Fig. 12. This could possibly be explained by the continuous reduction and oxidation reactions. For example, the reduction and oxidation of spinels have been extensively studied [59–61] and found to be driven by cation diffusion. Under oxidizing conditions, Fe_2O_3 is formed, which has a corundum structure with Fe^{3+} in octahedral sites. This means that at the outermost surface, where O_2-availability is high, the reduced phase Fe_3O_4 will be oxidized to Fe_2O_3. Fe_3O_4 has a spinel structure with Fe^{2+} in octahedral sites and Fe^{3+} cations equally distributed on tetrahedral and octahedral sites. When Fe_3O_4 is oxidized, Fe^{2+} is converted to Fe^{3+}, and vacancies appear in the octahedral sublattice. It is then possible for Cu to occupy these empty octahedral sites forming $CuFe_2O_4$. It is observed in Fig. 12 that the Fe-intensity is higher in the pores of the particle, while Ti and Ca intensities are lower. This suggests the formation of iron oxides and at higher reduction potentials, for example inside the particles, $CuFe_2O_4$ is not stable and will form $Cu_2Fe_2O_4$ and eventually Cu (s).

Table 3 shows that Pb is predominantly found in the fly ash and fairly equally distributed between the magnetic accept and reject ashes. Both Pb-silicates, Pb-titanates and chlorides were identified experimentally. To a large extent, Pb enters the gas phase in the form of $PbCl_2$, and some interactions with the bed material occur along its path to the fly ash. Pb titanates were not predicted in the global thermodynamic calculations, suggesting that local variations in the boiler could be significant.

The presented thermodynamic results regarding Cr show that it is not affected by any parameter. Chemical mapping of particle surfaces showed pieces of Cr-Ni-Fe-oxides, which are most likely the reason for the enrichment of Cr in the magnetic bottom ash fraction.

4.1. Implications for operation

It has been shown in this paper that the presence of oxygen carriers affects the ash chemistry and trace element distribution. Furthermore, the choice of bed material could increase the risk of agglomeration. For example, in Fig. 2, one may observe the formation of a molten phase for a silica sand bed already at 850 °C. The amount of slag phase is reduced when the silica sand bed is mixed with ilmenite. On the one hand, the slag phase shows a propensity to fixate lead and copper (and alkalis), which was observed in the chemical mappings, Figs. S17 and S18. This could result in fewer metal and alkali chlorides in the gas phase, which can positively affect corrosion and deposition. On the other hand, the melt could cause agglomeration and defluidization of the bed. Furthermore, high concentrations of Cl in the fuel will diminish the slag phase's potential benefit since metal chloride formation will be favored. For silica sand, mixed and ilmenite bed, the slag phase occupies over 15

wt% of the total phases above 850 °C, 900 °C and 1050 °C respectively as predicted by equilibrium. The amount of slag phase is the lowest in an ilmenite bed, meaning that higher temperatures can be reached without causing melt formation compared with other bed materials. Thermodynamic findings in this paper suggest that when utilizing ilmenite during OCAC:

- The operating temperature can be higher compared with silica sand before experiencing melt formation.
- An increase in temperature will aid the formation of gaseous metal chlorides (especially Pb and Cu), however, melts forming above 950 °C could retain part of these elements in the bed. Over 15 wt% of Zn dissolves in this melt when reaching 1050 °C.
- Increased fuel Cl-concentrations will favor the formation of gaseous $(CuCl)_x$ and $PbCl_2$, while increased S-concentrations could be beneficial for dissolving part of PbO in the melt. The Zn distribution was not affected by changes in S and was slightly affected by Cl.

The results in this paper obtained for different reduction potentials could provide insights on the phase formation in CLC. CLC is realized by a dual fluidized bed setup utilizing oxygen carriers (OCs) for oxygen transport between two reactors, the fuel reactor (FR) and air reactor (AR) [62]. In the FR, OCs are reduced by the fuel and then transported to the AR, which uses air to oxidize the OC. This results in a slight temperature difference where the AR is generally 50 °C higher [62]. Since no air is fed to the FR, the reduction potential will be higher compared with OCAC. According to studies simulating conditions in the FR, the reduction potential is estimated to be $\log_{10}[pCO/pCO_2] = -2$ [42]. In this paper, 850 °C was used to study the variation in reduction potential. A temperature change could affect the number of gaseous species, and thus more research is required in this field.

Nevertheless, the results presented here provide an insight into possible phase formation in a FR. Looking at the phase distribution of Pb, Cr, Cu and Zn one may observe that Pb can be expected to be volatilized entirely, mainly as PbS (g), which is not as corrosive as chlorides. This implies that the AR will avoid $PbCl_2$ and thereby corrosive attacks on heat transfer surfaces. In the FR, Cu is expected to form Cu_2S primarily, and the majority of Zn will form solid $Ca_2ZnSi_2O_7$ and $Zn(Cr, Ni)_2O_4$ with some gaseous Zn (g). Cr, however, is not expected to volatilize and is more persistent to changes in different parameters. In the FR, chromium could form the spinel $(Fe, Zn)Cr_2O_4$. In the AR, the primary phase will be corundum Cr_2O_3 suggesting that Cr will remain in the bottom bed during CLC operation. Concentrating heavy metals in the gaseous phase in the FR could potentially aid the extraction of these elements.

5. Conclusion

The fate of important trace elements has been investigated during Oxygen Carrier Aided Combustion (OCAC) of waste. Using a combination of thermodynamic modeling and detailed solid-state characterization of a substantial number of samples, it was possible to obtain a good view of the fate of Cu, Zn, Pb and Cr. It is shown that the presence of oxygen carriers affects the trace element distribution. This study found that when ilmenite is utilized during OCAC, it will increase the concentration of Zn, Cr and Cu in the magnetic separated bottom ashes. The enrichment is observed due to the i) incorporation of Zn in between the double Ca layer in the form of zinc ferrites, ii) accumulation of Cu inside the ilmenite particles also in the form of ferrites, and iii) formation of Cr oxides. The influence of ilmenite was not as evident for Pb, which is primarily concentrated in the fly ash.

The influence of temperature, reduction potential and fuel composition and their implications on operation have been discussed in detail. On the one hand, a temperature increase promotes the formation of a slag phase and gaseous metal chlorides, which are precursors for corrosion. On the other hand, the slag phase formed above 950 °C could retain part of these elements in the bed. Furthermore, the addition of sulfur could decrease the volatilization of Pb. Thermodynamic equilibrium calculations show that an ilmenite bed is less prone to slag formation compared with beds including silica sand.

CRediT authorship contribution statement

Ivana Staničić: Writing – original draft, Methodology, Investigation, Formal analysis, Visualization. **Rainer Backman:** Supervision, Writing - review & editing, Validation. **Yu Cao:** Supervision, Writing - review & editing, Validation. **Magnus Rydén:** Supervision, Writing - review & editing, Validation. **Jesper Aronsson:** Resources, Writing - review & editing. **Tobias Mattisson:** Supervision, Methodology, Conceptualization, Writing - review & editing.

Declaration of Competing Interest

The authors declare that they have no known competing financial interests or personal relationships that could have appeared to influence the work reported in this paper.

Acknowledgment

This work was financed by Formas, the Swedish Research Council for Environment, Agricultural Sciences and Spatial Planning (2017-01095), Improbed AB and The Swedish Energy Agency (46450-1). E.ON Händelö in Norrköping, Sweden is acknowledged for their collaboration. Special thanks to Fredrik Lind and Anders Lyngfelt for their help and support. This work was performed in part at the Chalmers Material Analysis Laboratory, CMAL.

Appendix A. Supplementary data

Supplementary data to this article can be found online at https://doi.org/10.1016/j.fuel.2021.122551.

References

[1] IPCC. Climate Change 2014: Mitigation of Climate Change. Contribution of Working Group III to the Fifth Assessment Report of the Intergovernmental Panel on Climate Change. In: Edenhofer O, Pichs-Madruga R, Sokona Y, Farahani E, Kadner S, Seyboth K, et al., editors. Cambridge, United Kingdom and New York, USA2014.
[2] IPCC. Summary for policymakers. In: Masson-Delmotte V, Zhai P, Pörtner HO, Roberts D, Skea J, Shukla PR, editors. Global warming of 1.5°C. An IPCC Special Report on the impacts of global warming of 1.5°C above pre-industrial levels and related global greenhouse gas emission pathways, in the context of strengthening the global response to the threat of climate change, sustainable development, and efforts to eradicate poverty, Geneva, Switzerland; 2018.
[3] Barker T, Bashmakov I, Bernstein L, Bogner JE, Bosch PR, Dave R. Technical summary. In: Metz B, Davidson OR, Bosch PR, Dave R, Meyer LA, editors. Climate Change 2007: Mitigtion. Contribution of Working Group III to the Fourth Assessment Report of the Intergovernmental Panel on Climate Change. Cambridge, United Kingdom and New York, NY, USA: Cambridge University Press; 2007.
[4] IPCC. Climate change 2013: the physical science basis. In: Stocker TF, Qin D, Plattner G-K, Tignor M, Allen SK, Boschung J, editors. Contribution of Working Group I to the Fifth Assessment Report of the Intergovern-mental Panel on Climate Change. Cambridge, United Kingdom and New York, NY, USA: Cambridge University Press; 2013. p. 1535.
[5] Kormi T, Bel Hadj Ali N, Abichou T, Green R. Estimation of landfill methane emissions using stochastic search methods. Atmos Pollut Res 2017;8(4):597–605.
[6] Eurostat. Municipal waste by waste management operations. Dataset: ENV_WASMUN: European Commission.
[7] Khandelwal H, Dhar H, Thalla AK, Kumar S. Application of life cycle assessment in municipal solid waste management: a worldwide critical review. J Cleaner Prod 2019;209:630–54.
[8] Sharma KD, Jain S. Municipal solid waste generation, composition, and management: the global scenario. Soc Responsibility J 2020;16(6):917–48.
[9] Lam CHK, Ip AWM, Barford JP, McKay G. Use of Incineration MSW Ash: A Review. Sustainability; 2010, p. 2.
[10] Gasser T, Guivarch C, Tachiiri K, Jones CD, Ciais P. Negative emissions physically needed to keep global warming below 2°C. Nat Commun. 2015;6.
[11] Azar C, Lindgren K, Obersteiner M, Riahi K, van Vuuren DP, den Elzen KMGJ, et al. The feasibility of low CO2 concentration targets and the role of bio-energy with carbon capture and storage (BECCS). Clim Change 2010;100(1):195–202.
[12] Svensk Avfallshantering 2019. Avfall Sverige; 2019.

[13] Moldenhauer P, Rydén M, Mattisson T, Lyngfelt A. Chemical-looping combustion and chemical-looping with oxygen uncoupling of kerosene with Mn- and Cu-based oxygen carriers in a circulating fluidized-bed 300 W laboratory reactor. Fuel Process Technol 2012;104:378–89.
[14] Lind F, Corcoran A, Andersson B, Thunman H. 12,000 hours of operation with oxygen-carriers in industrially relevant scale (75,000 kWth). VGB PowerTech; 2017.
[15] This is Improbed™ - improbed. Malmö, Sweden.
[16] Thunman H, Lind F, Breitholtz C, Berguerand N, Seemann M. Using an oxygen-carrier as bed material for combustion of biomass in a 12-MWth circulating fluidized-bed boiler. Fuel 2013;113:300–9.
[17] Moldenhauer P, Gyllén A, Thunman H, Lind F. A scale-up project for operating a 115 MWth biomass-fired CFB boiler with oxygen carriers as. Bed Mater 2018.
[18] Elled A-L, Åmand L-E, Eskilsson D. Fate of zinc during combustion of demolition wood in a fluidized bed boiler. Energy Fuels 2008;22(3):1519–26.
[19] Kinnunen H, Hedman M, Lindberg D, Enestam S, Yrjas P. Corrosion in recycled wood combustion—reasons, consequences, and solutions. Energy Fuels 2019;33(7):5859–66.
[20] Mattisson T, Keller M, Linderholm C, Moldenhauer P, Rydén M, Leion H, et al. Chemical-looping technologies using circulating fluidized bed systems: Status of development. Fuel Process Technol 2018;172:1–12.
[21] Bao J, Li Z, Cai N. Interaction between iron-based oxygen carrier and four coal ashes during chemical looping combustion. Appl Energy 2014;115:549–58.
[22] Rubel A, Zhang Y, Liu K, Neathery J. Effect of ash on oxygen carriers for the application of chemical looping combustion. Oil Gas Scie Technol 2011;66:291–300.
[23] Azis MM, Leion H, Jerndal E, Steenari BM, Mattisson T, Lyngfelt A. The effect of bituminous and lignite ash on the performance of ilmenite as oxygen carrier in chemical-looping combustion. Chem Eng Technol 2013;36:1460–8.
[24] Ilyushechkin AY, Kochanek M, Lim S. Interactions between oxygen carriers used for chemical looping combustion and ash from brown coals. Fuel Process Technol 2016;147:71–82.
[25] Siriwardane R, Tian H, Richards G, Simonyi T, Poston J. Chemical-looping combustion of coal with metal oxide oxygen carriers. Energy Fuels 2009;23(8):3885–92.
[26] Cheng D, Yong Q, Zhao Y, Gong B, Zhang J. Study on the interaction of the fe-based oxygen carrier with ashes. Energy Fuels 2020;34(8):9796–809.
[27] Bao J, Li Z, Cai N. Promoting the reduction reactivity of ilmenite by introducing foreign ions in chemical looping combustion. Ind Eng Chem Res 2013;52(18):6119–28.
[28] Vigoureux M, Knutsson P, Lind F. Sulfur uptake during oxygen-carrier-aided combustion with ilmenite. Energy Fuels 2020;34(6):7735–42.
[29] Corcoran A, Marinkovic J, Lind F, Thunman H, Knutsson P, Seemann M. Ash properties of ilmenite used as bed material for combustion of biomass in a circulating fluidized bed boiler. Energy Fuels 2014;28(12):7672–9.
[30] Corcoran A, Knutsson P, Lind F, Thunman H. Mechanism for migration and layer growth of biomass ash on ilmenite used for oxygen carrier aided combustion. Energy Fuels 2018;32(8):8845–56.
[31] Gyllén A, Knutsson P, Lind F, Thunman H. Magnetic separation of ilmenite used as oxygen carrier during combustion of biomass and the effect of ash layer buildup on its activity and mechanical strength. Fuel 2020;269:117470. https://doi.org/10.1016/j.fuel.2020.117470.
[32] Backman R, Hupa M, Hiltunen M, Peltola K. Interaction of the behavior of lead and zinc with alkalis in fluidized bed combustion or gasification of waste derived fuels. 18th International Conference on Fluidized Bed Combustion. 2005.
[33] Khan AA, de Jong W, Jansens PJ, Spliethoff H. Biomass combustion in fluidized bed boilers: Potential problems and remedies. Fuel Process Technol 2009;90(1):21–50.
[34] Cottis B, Graham M, Lindsay R, Lyon S, Richardson T, Scantlebury D, editors. Spiegel M. 1.14 - Corrosion in Molten Salts. Shreir's Corrosion. Oxford: Elsevier; 2010. p. 316–30.
[35] Niu Y, Tan H, Hui S. Ash-related issues during biomass combustion: Alkali-induced slagging, silicate melt-induced slagging (ash fusion), agglomeration, corrosion, ash utilization, and related countermeasures. Prog Energy Combust Sci 2016;52:1–61.
[36] Abanades S, Flamant G, Gagnepain B, Gauthier D. Fate of heavy metals during municipal solid waste incineration. Waste Manage Res 2002;20(1):55–68.
[37] Pedersen AJ, van Lith SC, Frandsen FJ, Steinsen SD, Holgersen LB. Release to the gas phase of metals, S and Cl during combustion of dedicated waste fractions. Fuel Process Technol 2010;91(9):1062–72.
[38] van Lith SC, Jensen PA, Frandsen FJ, Glarborg P. Release to the gas phase of inorganic elements during wood combustion. Part 2: influence of fuel composition. Energy Fuels 2008;22(3):1598–609.
[39] Hannl TK, Sefidari H, Kuba M, Skoglund N, Öhman M. Thermochemical equilibrium study of ash transformation during combustion and gasification of sewage sludge mixtures with agricultural residues with focus on the phosphorus speciation. Biomass Convers Biorefin 2021;11(1):57–68.
[40] Hildor F, Zevenhoven M, Brink A, Hupa L, Leion H. Understanding the interaction of potassium salts with an ilmenite oxygen carrier under dry and wet conditions. ACS Omega 2020;5(36):22966–77.
[41] Yilmaz D, Steenari B-M, Leion H. Comparative study: impacts of Ca and Mg salts on iron oxygen carriers in chemical looping combustion of biomass. ACS Omega 2021;6(25):16649–60.
[42] Staničić I, Hanning M, Deniz R, Mattisson T, Backman R, Leion H. Interaction of oxygen carriers with common biomass ash components. Fuel Process Technol 2020;200:106313. https://doi.org/10.1016/j.fuproc.2019.106313.
[43] Dai J, Hughey L, Whitty KJ. Influence of fuel ash on the recoverability of copper from the spent material of chemical looping combustion. Fuel Process Technol 2020;201:106358. https://doi.org/10.1016/j.fuproc.2020.106358.
[44] Konttinen J, Backman R, Hupa M, Moilanen A, Kurkela E. Trace element behavior in the fluidized bed gasification of solid recovered fuels – a thermodynamic study. Fuel 2013;106:621–31.
[45] Kramb J, Konttinen J, Backman R, Salo K, Roberts M. Elimination of arsenic-containing emissions from gasification of chromated copper arsenate wood. Fuel 2016;181:319–24.
[46] Becidan M, Sørum L, Lindberg D. Impact of municipal solid waste (MSW) quality on the behavior of alkali metals and trace elements during combustion: a thermodynamic equilibrium analysis. Energy Fuels 2010;24(6):3446–55.
[47] Enestam S, Backman R, Mäkelä K, Hupa M. Evaluation of the condensation behavior of lead and zinc in BFB combustion of recovered waste wood. Fuel Process Technol 2013;105:161–9.
[48] Staničić I, Mattisson T, Backman R, Cao Yu, Rydén M. Oxygen carrier aided combustion (OCAC) of two waste fuels - experimental and theoretical study of the interaction between ilmenite and zinc, copper and lead. Biomass Bioenergy 2021;148:106060. https://doi.org/10.1016/j.biombioe.2021.106060.
[49] Arm M, Lindeberg J, Rodin Å, Öhrström A, Backman R, Öhman M, et al. Gasbildning i Aska. In: AB VS, editor. MillLJÖRIKTIG ANVÄNDNING AV ASKOR 9572006.
[50] Moulder JM, Stickle WF, Sobol PE, Bomben Kd. Handbook of X-ray Photoelectron spectroscopy - a reference book of standard spectra for identification and interpretation of XPS Data. 6509 flying cloud drive Eden Prairie, Minnesota 55344 United Stales of America: Perkin-Elmer Corporation - Physical Electronics Division; 1992.
[51] Naumkin VA, Kraut-Vass A, Gaarenstroom SW, Powell CJ. NIST X-ray Photoelectron Spectroscopy Database - NIST Standard Reference Database 20, Version 4. 6 June 2000 ed. Gaithersburg MD, 20899: National Institute of Standards and Technology; 2012.
[52] Determination of the fossil carbon content in combustible municipal solid waste in Sweden. Avfall Sverige Utveckling Report U2012:02; 2012.
[53] Frandsen FJ, Pedersen AJ, Hansen J, Madsen OH, Lundtorp K, Mortensen L. Deposit formation in the FASAN WtE boiler as a function of feedstock composition and boiler operation. Energy Fuels 2009;23(7):3490–6.
[54] Bale CW, Bélisle E, Chartrand P, Decterov SA, Eriksson G, Gheribi AE, et al. FactSage thermochemical software and databases - 2010–2016. Calphad 2016;54:35–53.
[55] Roine A. HSC Chemistry® [Software]. Pori: Outotec; 2018.
[56] Abián M, Abad A, Izquierdo MT, Gayán P, de Diego LF, García-Labiano F, et al. Titanium substituted manganese-ferrite as an oxygen carrier with permanent magnetic properties for chemical looping combustion of solid fuels. Fuel 2017;195:38–48.
[57] Billen P, Van Caneghem J, Vandecasteele C. Predicting melt formation and agglomeration in fluidized bed combustors by equilibrium calculations. Waste Biomass Valorization 2014;5(5):879–92.
[58] Karamat S, Rawat RS, Lee P, Tan TL, Ramanujan RV. Structural, elemental, optical and magnetic study of Fe doped ZnO and impurity phase formation. Progress Nat Sci: Mater Int 2014;24(2):142–9.
[59] Jozwiak WK, Kaczmarek E, Maniecki TP, Ignaczak W, Maniukiewicz W. Reduction behavior of iron oxides in hydrogen and carbon monoxide atmospheres. Appl Catal A 2007;326(1):17–27.
[60] Sidhu PS, Gilkes RJ, Posner AM. Mechanism of the low temperature oxidation of synthetic magnetites. J Inorg Nucl Chem 1977;39(11):1953–8.
[61] Ketteler G, Weiss W, Ranke W, Schlögl R. Bulk and surface phases of iron oxides in an oxygen and water atmosphere at low pressure. Phys Chem Chem Phys 2001;3(6):1114–22.
[62] Pröll T. 10 - Fundamentals of chemical looping combustion and introduction to CLC reactor design. In: Fennell P, Anthony B, editors. Calcium and Chemical Looping Technology for Power Generation and Carbon Dioxide (CO2) Capture. Woodhead Publishing; 2015. p. 197–219.